INTERNATIONAL JOURNAL OF HYDROGEN ENERGY XXX (2016) 1–21

Available online at www.sciencedirect.com

ScienceDirect

journal homepage: www.elsevier.com/locate/he

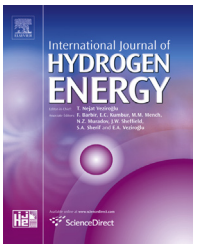

Numerical analysis on steam methane reforming in a plate microchannel reactor: Effect of washcoat properties

Chenxi Cao, Nian Zhang, Yi Cheng *

Beijing Key Laboratory of Green Reaction Engineering and Technology, Department of Chemical Engineering, Tsinghua University, Beijing 100084, PR China

ARTICLE INFO

Article history:
Received 15 February 2016
Received in revised form
6 September 2016
Accepted 7 September 2016
Available online xxx

Keywords:
Steam methane reforming
Microchannel reactor
CFD with microkinetics
Washcoat thickness
Pore diameter and porosity

ABSTRACT

The effect of washcoat properties is theoretically investigated for steam methane reforming (SMR) in a plate microchannel reactor. Transport phenomena and reaction within the catalytic washcoat and in the bulk gas phase are modeled using a two-dimensional, comprehensive CFD model with fully resolved catalytic washcoat, coupled with detailed chemistry for SMR over Ni catalyst. Simulation results show that the process is governed by internal mass transfer and reaction, therefore the reactor performance depends markedly on the washcoat structure and dimension. Increasing pore size of the washcoat leads to improved heat coupling, which lowers the hotspot temperature and reduces axial temperature gradients. In the meantime, the role of porosity remains trivial. Further, using a thicker washcoat carrying a greater loading of catalyst can considerably increase the reactor throughput within washcoat thickness of 75 μm, at the expense of certain loss of the catalyst productivity. Optimized washcoat properties would rely on the catalyst activity, price and specific product demand.

Introduction

Steam methane reforming (SMR) remains the world's largest source of industrial hydrogen up to now since its first commercialization over 80 years ago. In centralized plants, this highly endothermic reaction is carried out catalytically in tubular fixed-bed reactors that are placed in gas-fueled furnaces, under high pressure (>20 atm) and temperature (800–900 °C), but with a comparatively slow rate (the residence time is a few seconds) [1]. Despite the fact that industrial technology for SMR is well-established, several downsides are unavoidable; these involve poor heat-transfer from the furnace to the catalyst inside the tube, intraparticle heat and mass transfer limitations [2], and catalyst deactivation [3,4]. The unfavorable energy and matter utilization and the reactor-furnace configuration result in a rather bulky process and a large plant size.

Down-scaling of SMR has been a pressing demand over the last two decades in view of the world's ever growing need for cleaner, safer and more economical hydrogen production processes. Microchannel reactors naturally fit these needs owing to process intensification via miniaturization, which tremendously increases transport rates [5], allowing for processes running at almost the intrinsic rate of chemical kinetics. Regarding SMR, another attraction offered by microchannel reactor is catalytic combustion assisted reforming, in which the proximity of the heat source and heat

* *Corresponding author*. Fax: +86 10 62772051.
E-mail address: yicheng@tsinghua.edu.cn (Y. Cheng).

http://dx.doi.org/10.1016/j.ijhydene.2016.09.034
0360-3199/

sink benefits a highly integrated and efficient reformer system. Such compact systems find emerging applications in distributed and localized hydrogen/syngas production, including portable fuel cell systems [6], hydrogen fueling stations [7], small-scale GTL process [8] and so on. The overwhelming prospects and feasibility of SMR based on microchannel reactor has been well demonstrated by the leading work of Velocys® Inc. and PNNL [9–11].

Yet process intensification achieved by microchannel reactor is challenging in the context of precisely matching the design to specific process conditions. For instance, SMR can happen over different catalyst systems. Ni, the industrial catalyst, is robust and inexpensive, but relatively easy to deactivate due to carbon deposition and sulfur poisoning [12]. Thus, it dictated prior sulfur removal and high steam to carbon (S/C) ratios on stream, which decrease both the system's energy efficiency and compactness. Rh and other noble metals (Ru, Pd) are orders of magnitude more active for SMR, less prone to coking, and possess high sulfur tolerance, but their expensiveness requires careful usage in a small amount. The point is that process and catalyst intensification must be symbiotic for a downscaled reformer [13]. For washcoated catalyst in microchannel reactor, this intensification implies optimizing both the catalyst's active phase and the porous washcoat (support). For partial oxidation on Rh in monolithic reactors, Stutz and Poulikakos [14] have demonstrated marked effect of washcoat properties and the existence of an optimum washcoat thickness. Similarly, washcoat effect proved to be significant for CO preferential oxidation on Pt in foam-based or honeycomb reactors [15]. Although Stefanidis and Vlachos [16] suggested that Rh-based SMR in microchannel reactor is reaction-controlled, their modeling approach has lumped internal mass transfer and catalytic reaction. Given that partial oxidation is a combination of combustion and SMR [17], it is very likely that effect of washcoat properties is also crucial for SMR in microchannel reactor. That is, despite the fact that the washcoat dimension is considerably small (typically 10–100 μm), intra washcoat mass transfer resistance is significant and not negligible for fast reactions as SMR.

Quantifying the mass transfer resistance for washcoated catalyst in microscale devices is difficult by experimental approach, with which only the overall conversion/yield can be easily measured – which is insufficient for verifying the effect of washcoat properties. Also required are efforts to precisely control and tune the washcoat properties (such as thickness, pore size, etc.) as needed in experiments. These difficulties can be readily overcome, however, by numerical simulation. So far, various modeling schemes have been available for modeling SMR at microscale, ranging from the simplest one-dimensional, plug flow models to three-dimensional, full CFD models [18–24]. To couple gas-phase chemistry and surface catalytic reaction, the instantaneous diffusion approach is the most efficient strategy, which does not necessitate resolving the washcoat geometry; the most sophisticated approach is to solve full reaction-diffusion equations for the catalyst domain. A comprehensive review regarding these approaches can be found in Ref. [25]. Although Irani et al. [26] argued whether the surface-based (instantaneous diffusion approach) or volume-based (solving reaction-diffusion equation) models are preferred for SMR on Ni in a monolithic reactor, Mladenov et al. has shown that for catalytic converters, the latter approach best agrees with the experimental data, and allows discrimination between intrinsic kinetics and mass transfer effects [27]. Anyhow, simulation aiming at optimization of washcoat properties should be washcoat-resolved, if not necessarily. To our best knowledge, most modeling work on SMR in microchannel reactor is limited to the instantaneous diffusion approach. Although some simulations resolved the washcoat geometry [22,28–31], they scarcely discussed the effect of washcoat properties. Another major limitation of the current modeling work is that, with rare exceptions [23,32,33], they used global kinetic models such as that of Xu and Froment [34]. Global kinetics accounts for overall reaction and is deduced with *a priori* assumptions (e.g., the rate-determining step and the most abundant reactive intermediates), which may be invalid under various real reaction conditions. Microkinetics, on the other hand, is developed bottom-up without using condition-dependent assumptions. It can capture behaviors of the reacting system over a wide range of operating conditions. Such reliable detailed chemistry models have been successfully applied in our previous work [35–37].

The objective of this work is to explore the effect of washcoat properties on the performance of a plate microchannel reactor for SMR theoretically. Unlike the aforementioned simulation work, a detailed, washcoat-resolved approach is adopted for momentum, heat and mass transfer within the catalytic washcoat, while catalytic reactions are described by a reliable microkinetics model. We study the basics of reaction and mass transfer within the washcoat, and perform a parametric study with respect to washcoat properties, such as thickness, pore size and porosity. Guidelines for optimization of washcoat are sketched in the context of the reactor's thermal behavior, the catalyst productivity and the reactor throughput.

Mathematical model

An integrated plate microchannel reactor for SMR was modeled with a two-dimensional comprehensive CFD model in which the washcoat was resolved with finite thickness. Catalytic reforming was modeled with microkinetics. Computational domains were specified for a structural unit model and a reduced, single-channel model. Appropriate governing equations, boundary conditions and chemical kinetics were applied for the gas phase, the solid wall and the porous washcoat. This modeling scheme made use of no lumped, correlated transport coefficients. All model parameters were set *a priori* instead of by fitting experimental data. An effective solution method was proposed which iteratively solve the set of differential-algebraic equations forming the mathematical model, ensuring good convergence. All these aspects with regards to establishing the mathematical model are detailed in the following sections.

Model geometries and computational domains

The microchannel reactor is composed of alternate, parallel reforming and heating channels with metal walls in between.

Please cite this article in press as: Cao C, et al., Numerical analysis on steam methane reforming in a plate microchannel reactor: Effect of washcoat properties, International Journal of Hydrogen Energy (2016), http://dx.doi.org/10.1016/j.ijhydene.2016.09.034

Endothermic SMR happens over Ni catalyst coated on the reforming side of the wall surface, driven by heat conducted through the wall from the adjacent heating channel. In the heating channels, either catalytic combustion (over wall-coated Pt/Pd catalyst) or hot inert gas flow (e.g., flue gas) is employed for heat supply.

Fig. 1 shows the two-dimensional model geometries used in simulation. They represent the constituting elements of the integrated microchannel reactor [36], based on the assumption that an inlet gas distributor assures an equal partitioning of the feedstock. For modeling the plate-type structured catalyst [38], the two-dimensional approach is reasonable, as the channels are flat so that the gradients in the width direction are insignificant. Fig. 1a is the geometry of the structural unit model, which consists of one reforming channel, one heating channel and the metal wall between them. The corresponding computational domain includes two free fluid regions (the channels), one porous media region (the reforming catalytic washcoat), and one solid region (the metal wall). Since our interest is concentrated on the reforming performance, catalytic combustion was treated as a wall reaction so that the combustion catalytic washcoat geometry was not resolved (zero-thickness, by using the instantaneous diffusion approach). Only one-half of each channel was incorporated into the computational domain by applying a symmetric boundary condition. An insulated blank region was added upstream the inlet and downstream the outlet of the channels to ensure better convergence [35]. Fig. 1b is the geometry of the reduced, single-channel model, which involves one reforming channel only. Correspondingly, in the computational domain are one free fluid region and one porous media region. It could be viewed as a part of the structural unit model.

Governing equations and physical property calculations

Development of the governing equations depends on the following assumptions:

a) The width of the reaction channel is significantly larger than the height;
b) The flow in the reaction channel is laminar;
c) Steady-state operation of the reactor has been reached;
d) Gas-mixture can be treated as incompressible ideal gas (the density of the mixture can be calculated from ideal gas law);
e) Gas phase non-catalytic reaction can be neglected;
f) The porous catalytic washcoat is isotropic and in local thermal equilibrium with the gas mixture.

These assumptions are widely accepted, and were used in our previous modeling work concerning SMR in microchannel reactors [37,39], as well as in modeling other reactions taking place within the catalytic washcoat in a microchannel reactor [30,40].

Table 1 gives the governing equations for fluid flow and heat and mass transfer in the free fluid phase, the solid phase and the porous washcoat phase. For the free fluid phase, Knudsen number ($Kn = \lambda/D_h$) was evaluated to be less than 10^{-3} for the characteristic dimensions of the simulated reactor, thus the continuum assumption was valid. Therefore, general

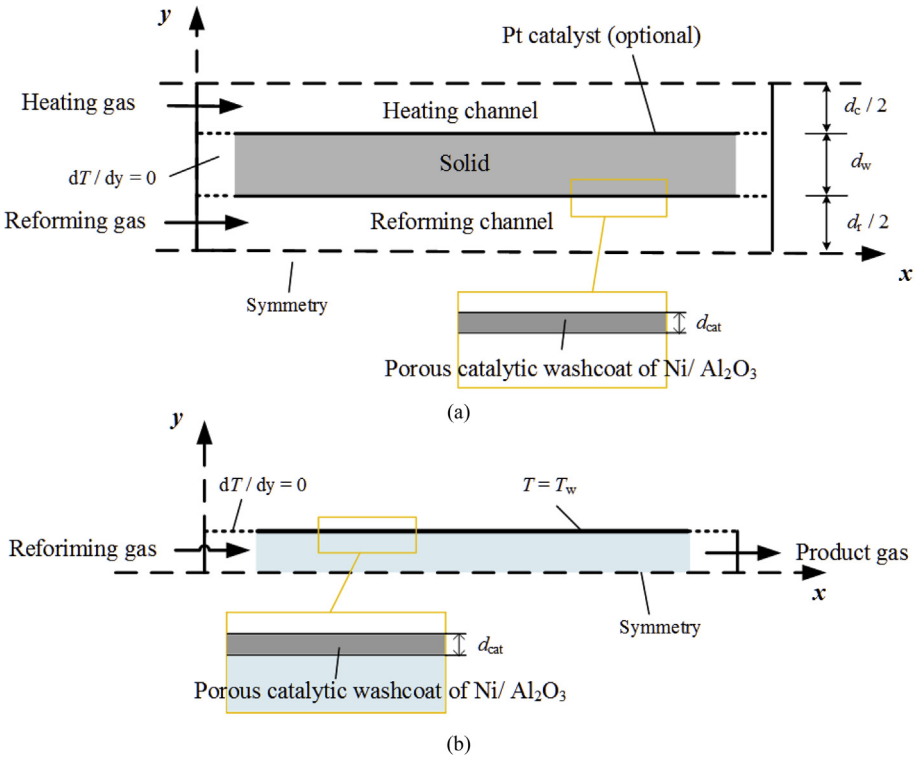

Fig. 1 – Computational domains for the simulated microchannel reactor SMR: (a) the structural unit model comprising a heating channel, a reforming channel and a metal wall in between; (b) the single channel model for a reforming channel only.

Please cite this article in press as: Cao C, et al., Numerical analysis on steam methane reforming in a plate microchannel reactor: Effect of washcoat properties, International Journal of Hydrogen Energy (2016), http://dx.doi.org/10.1016/j.ijhydene.2016.09.034

Table 1 – Governing equations used in the mathematical model of the simulated microchannel reactor.

Free-fluid

Continuity equation

$\nabla\cdot(\rho\mathbf{u}) = 0$

Navier–Stokes equations

$(\mathbf{u}\cdot\nabla)\rho\mathbf{u} = -\nabla P + \mu\nabla^2\mathbf{u}$

Energy equation

$\nabla\cdot[\rho\mathbf{u}(\sum_i Y_i h_i + |\mathbf{u}|^2)] = \nabla\cdot(k\nabla T - \sum_i h_i\mathbf{J}_i)$

Species equation

$\nabla\cdot(\rho Y_i\mathbf{u}) = \nabla\cdot[\rho(D_{i,M}\nabla Y_i + D_{i,T}\nabla T)]$

Solid wall

Energy equation

$\nabla\cdot(k\nabla T) = 0$

Catalytic washcoat

Continuity equation

$\nabla\cdot(\rho\mathbf{u}) = 0$

Forchheimer's modified formulation of Darcy Equations

$(\mathbf{u}\cdot\nabla)\rho\mathbf{u} = -\nabla P + \mu'\nabla^2\mathbf{u} - \frac{\mu}{\kappa}\mathbf{u} - \frac{C_2}{2}\rho|\mathbf{u}|\mathbf{u}$

Energy equation

$\nabla\cdot[\rho\mathbf{u}(\sum_i Y_i h_i + |\mathbf{u}|^2)] = \nabla\cdot(k_{eff}\nabla T - \sum_i h_i\mathbf{J}_i) + \sum_i h_i\widehat{R}_i$

Species equation

$\nabla\cdot(\rho Y_i\mathbf{u}) = \nabla\cdot[\rho(D_{i,eff}\nabla Y_i + D_{i,T}\nabla T)] + M_i\widehat{R}_i$

conservation equations of momentum, energy and mass transfer for continuous fluids were used. Gravity and other body-forces were ignored in the conservation equations since low-density gas fluid was simulated. In energy and species equations, the diffusive mass flux of each species ($\mathbf{J}_i$) was driven together by concentration and temperature gradients:

$$\mathbf{J}_i = -\rho(D_{i,M}\nabla Y_i + D_{i,T}\nabla T) \quad (i = 1, \ldots, N_g) \tag{1}$$

where $D_{i,M}$ and $D_{i,T}$ are the molecular and thermal diffusivities, respectively. Further, Brinkman number ($Br = \frac{\mu u^2}{k(T_w - T_0)}$) of the fluid was found in the order of 10^{-5}–10^{-3}. Hence, viscous heating was ignorable with respect to conductive and convective heat transfer. The dissipation term was then neglected in the energy equation.

The source term in momentum equations for the catalytic washcoat acts as a momentum sink, causing a pressure drop when fluids flow through the porous media. In this study homogeneous and isotropic porous media were hypothesized; the resulting momentum source term was written as

$$\mathbf{S}_M = -\frac{\mu}{\kappa}\mathbf{u} - \frac{C_2}{2}\rho|\mathbf{u}|\mathbf{u} \tag{2}$$

according to Brinkman–Forchheimer model [41]. μ is the dynamic viscosity of the fluid, κ is the permeability of the porous media, and C_2 is the inertial resistance factor of the porous media. The first and the second terms on the right-hand side of Eq. (2) stand for viscous and inertial momentum loss, respectively. Since the pore Reynolds number turned out to be much smaller than unity for all studied conditions, the inertial loss term was neglected by setting C_2 to zero.

Energy and mass source terms in the energy and species equations were taken into account for the catalytic washcoat phase only because we assume no homogeneous reactions. The source terms, R_i and S_H, describe the heat and mass changes due to chemical reactions:

$$S_H = \sum_i h_i\widehat{R}_i \quad (i = 1, \ldots, N_g + N_s) \tag{3}$$

$$R_i = M_i\widehat{R}_i \quad (i = 1, \ldots, N_g + N_s) \tag{4}$$

where $\widehat{R}_i$ is the creation/consuming rate of species i (molar) on a per washcoat volume basis, calculated from microkinetics (see Section Kinetic models for surface catalytic reactions); h_i is the molar enthalpy of species i.

All physical properties of the fluids in this study are temperature- and composition-dependent, as listed in Appendix 1. For the porous media, effective thermal conductivity was used which was expressed as the volume average of the fluid thermal conductivity and the solid thermal conductivity

$$k_{eff} = \varepsilon k_f + (1-\varepsilon)k_s \tag{5}$$

where ε is the porosity of porous media, k_f and k_s are the thermal conductivity of the fluid and solid phases of porous media, respectively.

A modified Fick model was used instead of the more complex Dusty Gas Model (DGM) in this study. The former is as accurate as DGM under diverse conditions of SMR, while being much less computationally expensive [42]. In the modified Fick model, effective diffusion within porous media was modeled with an equivalent (effective) Fickian diffusivity, $D_{i,eff}$, which was computed from molecular diffusivity, $D_{i,M}$, and Knudsen diffusivity, $D_{i,k}$, using a modified form of the Bosanquet formula [41]:

$$D_{i,eff} = \frac{\varepsilon}{\tau}\left(\frac{1 - \alpha_{i,M}Y_i}{D_{i,M}} + \frac{1}{D_{i,k}}\right)^{-1} \tag{6}$$

where ε is the porosity, and τ is the tortuosity of porous media. The molecular diffusivity of species i in the gas mixture was calculated from the Wilke equation [43].

$$\frac{1}{D_{i,M}} = \frac{1}{1 - Y_i}\sum_{j\neq i}\frac{Y_j}{D_{ij}} \tag{7}$$

where $\alpha_{i,M}$ was given in:

$$\alpha_{i,M} = 1 - \left(\frac{M_i}{M_{avg}}\right)^{1/2} \tag{8}$$

The formula of Knudsen diffusivity was [44]:

$$D_{i,k} = \frac{d_p}{3}\sqrt{\frac{8RT}{\pi M_i}} \tag{9}$$

where d_p is the mean pore diameter of porous media.

Kinetic models for surface catalytic reactions

The source terms in energy and species equations rely on the expression of reaction kinetics for each species involved. For SMR over Ni catalyst, microkinetics proposed by the Deutschmann group [45,46] was used in this work (see Table A.1 in the appendix). Involving 42 elementary reactions of 6 gas-phase species and 13 surface species, this reaction kinetics is applicable for a wide range of Ni-based catalysts [47].

Please cite this article in press as: Cao C, et al., Numerical analysis on steam methane reforming in a plate microchannel reactor: Effect of washcoat properties, International Journal of Hydrogen Energy (2016), http://dx.doi.org/10.1016/j.ijhydene.2016.09.034

In the kinetics the molar creation/consuming rate of species, i was calculated on a per catalytic surface area basis as:

$$\widehat{r}_i = \sum_{n=1}^{K_s} \nu_{i,n} k_n \prod_{j=1}^{N_g+N_s} [X_j]^{\nu_{j,n}} \quad (i = 1, \ldots, N_g + N_s) \tag{10}$$

where the rate constants of the nth reaction, k_n, were calculated by a modified Arrhenius equation,

$$k_n = AT^{\alpha,n} \exp\left(\frac{-E_{a,n}}{RT}\right) \prod_{i=1}^{N_s} \Theta_i^{\varphi_n} \exp\left(\frac{e_{i,n}\Theta_i}{RT}\right) \tag{11}$$

which accounts for the coverage dependence of surface reaction rates (by φ_n and $e_{i,n}$). In particular, the rate constants of adsorption reactions in Table A.1 were given in sticking coefficients γ, which could be converted to conventional rate constants by:

$$k_n = \frac{\gamma}{\Gamma^{\nu_n}} \sqrt{\frac{RT}{2\pi M_i}} \tag{12}$$

For the steady-state simulation considered, invariant surface coverage of each surface species was enforced:

$$\frac{\partial \Theta_i}{\partial t} = \frac{\widehat{r}_i}{\Gamma} = 0 \quad (i = 1, \ldots, N_s) \tag{13}$$

where the site density Γ for Ni catalyst (the number of active sites on the catalyst surface) was set as 2.6×10^{-9} mol cm^{-2} in the simulation.

The molar rate $\widehat{r}_i$ on a per surface area basis in Eq. (13) was converted to molar rate $\widehat{R}_i$ on a per catalytic volume basis by:

$$\widehat{R}_i = F_{cat} \delta_{cat} \rho_{cat} \widehat{r}_i \tag{14}$$

where F_{cat} is the active metal surface area of catalyst, δ_{cat} is the thickness of the catalytic washcoat, ρ_{cat} is the density of the catalytic washcoat.

To model catalytic combustion of methane, we used the global rate expressions for Pt catalyst developed by Trimm and coauthors [48,49]:

$$r_c = \frac{k_c P_{CH_4} P_{O_2}^{1/2}}{\left(1 + K_{CH_4}^C P_{CH_4} + K_{O_2}^C P_{O_2}^{1/2}\right)^2} \tag{15}$$

The parameters therein can be found in the references above. Catalytic combustion provides a certain pattern of heating profile, but the detail of kinetics is of minor importance. It was treated as a wall reaction with instantaneous diffusion, in which the catalyst loading and the effective usage of the internal surface area of catalyst were lumped by a constant factor [25], and the corresponding mass flux due to reaction is applied in the boundary condition of the wall. More details were described in our previous work [37,39].

Boundary conditions

The differential equations in the mathematical model were solved being subject to the boundary conditions listed in Table 2. Inlet boundaries of the channels were uniform velocity, which is equal to the average velocity calculated from the volumetric flow rate. Inlet diffusion of species was not considered. Outlet boundaries of the channels were constant static pressure (1 atm) and zero normal gradients of velocity, temperature, and species mass fraction.

Adiabatic wall conditions were imposed on the outer walls because the heat exchange between the reactor and environment is expected to be eliminated by suitable insulation. Symmetric boundaries were imposed on the centerlines of reaction channels. Specifically, in the reduced model, the wall condition of the reforming channel was constant temperature. This means under ideal conditions the reactor thermal management is perfect so that isothermal operation is achieved.

At the porous media solid wall interface where heat coupling has to be taken into account, thermally coupled and no-slip boundary conditions were applied. Although the Knudsen number for the porous media (~10^{-1}) is in the regime of slip boundary, applying the no-slip boundary is not expected to lead to visible deviation due to the negligible fluid velocity. At the free-fluid porous-media interface, continuity in the velocity, temperature, pressure and species mass fraction was held. The continuity is inherent in the applied Brinkman–Forchheimer model [41] for the momentum transport in porous media. Also the generally used stress-continuous condition was imposed at the interface; the against stress-jump condition only yields significantly different results when the porosity is high [50], which is not the case in this study.

Model parameters and operating conditions

Table 3 lists the reactor dimensions, material properties and the range of operating conditions used in the simulation. The channel lengths were fixed at 55 mm. The gap sizes of the channels were in the sub-millimeter range: the heating channel was 0.5 mm in height; the height of the reforming channel was 0.8 mm (the default) or 0.4 mm according to different cases in simulation. The metal wall was 1.0 mm thick. Its thermal conductivity was a fixed value of 20 W m^{-1} K^{-1}, representative of typical high-temperature alloy steels.

The current work concerns SMR under atmospheric pressure. The inlet line velocities of the reforming gas varied from 0.175 to 7.34 m/s, corresponding to GHSVs (based on the reaction channel volume) from 0.29×10^4 h^{-1} to 12.2×10^4 h^{-1} (at 298 K and 1 atm). The inlet line velocity of the fuel gas was fixed at 1.719 m/s (GHSV = 2.85×10^4 h^{-1}). The feed S/C ratio of the reforming channel was held at 3.0. The inlet CH_4: O_2 molar ratio was 1:2, and balance N_2 was introduced to maintain a fuel to reform volumetric flow ratio of 3.5.

Washcoat thickness in this work varied from 10 to 100 μm, which was considered typical for catalytic washcoat in microdevices. The washcoat thickness in our experiments is estimated to be 20–40 μm. With regard to pore structure parameters of the catalytic washcoat, typical porosity was reported to be around 0.5 [51], which was made the default in this work. The tortuosity usually lies in the range of 3–4 [27], herein it was set to 3. For the pore size of porous washcoat, unlike some simulation work [22,31] in which a pore diameter around 300 nm was set according to the industrial Ni catalyst [52], we used a default value of 20 nm, which is close to the

Please cite this article in press as: Cao C, et al., Numerical analysis on steam methane reforming in a plate microchannel reactor: Effect of washcoat properties, International Journal of Hydrogen Energy (2016), http://dx.doi.org/10.1016/j.ijhydene.2016.09.034

Table 2 – Boundary conditions for the mathematical model.

Channels
Inlets
$u_x = u_0,\ u_y = 0;\ T = T_0;\ Y_i = Y_{i,0}$
Outlets
$\frac{\partial \mathbf{u}}{\partial x} = 0;\ \frac{\partial T}{\partial x} = 0;\ P = P_0;\ \frac{\partial Y_i}{\partial x} = 0$
Walls
Adiabatic wall
$\mathbf{u} = 0;\ \frac{\partial T}{\partial \mathbf{n}} = 0;\ \frac{\partial Y_i}{\partial \mathbf{n}} = 0$
Heating wall (in single channel model)
$\mathbf{u} = 0;\ T = T_w;\ \frac{\partial Y_i}{\partial \mathbf{n}} = 0$
Symmetry
$\frac{\partial \mathbf{u}}{\partial \mathbf{n}} = 0;\ \frac{\partial T}{\partial \mathbf{n}} = 0;\ \frac{\partial Y_i}{\partial \mathbf{n}} = 0$
Interfaces
Free-fluid - porous medium
$\mathbf{u}_f = \mathbf{u}_p;\ T_f = T_p;\ P_f = P_p;\ Y_{i,f} = Y_{i,p}$
Porous medium – solid wall
$\mathbf{u}_p = 0;\ k_{eff}\frac{\partial T_f}{\partial y} = k_w\frac{\partial T_w}{\partial y};\ \frac{\partial Y_{i,p}}{\partial y} = 0$

Table 3 – Model parameters and operating conditions.

Free-fluid	Reforming channel	Heating channel
Channel height (mm)	0.8 (0.4, 0.8)[a]	0.5
Channel length (mm)	55	55
Inlet temperature (K)	1173 (873–1173)	1173
Wall temperature (in reduced model, K)	1173 (873–1173)	–
Operation pressure (atm)	1	1
Inlet velocity (m/s)	0.887 (0.175–7.34)	1.719
Inlet composition (vol.)	25% CH_4 75% H_2O	5.9% CH_4 11.8% O_2 balance N_2
Solid wall		
Thickness (mm)	1.0 mm	
Thermal conductivity ($W\cdot m^{-1}\cdot K^{-1}$)	20	
Catalytic washcoat		
Thickness (μm)	25 (10–100)	
Porosity	0.5 (0.35–0.7)	
Tortuosity	3	
Pore diameter (nm)	20 (2.5–50)	
Thermal conductivity (γ-Al_2O_3, $W\cdot m^{-1}\cdot K^{-1}$)	6.5	
Density (γ-Al_2O_3, $kg\cdot m^{-3}$)	3970	
Active Ni surface area of catalyst ($m^2\cdot g^{-1}$)	4.1 (0.44–8.75)	
Permeability (m^2)	10^{-16} (10^{-8}–10^{-16})	

[a] The number before the bracket is the default value, while the ones in the bracket denote the range within which the specific variable is varied in simulation.

reported value of 10 nm for the Pt/Al_2O_3 washcoat in monolith [53].

The density of the catalytic washcoat was calculated by mass balance as

$$\rho_{cat} = \rho_{\gamma-Al_2O_3}\frac{1-\varepsilon}{1-w_{NiO}\%} \quad (16)$$

where $w_{NiO}\%$ was the metal content of the supported catalyst. For example, taking $\rho_{\gamma-Al_2O_3} = 3970\ kg\ m^{-3}$, $\varepsilon = 0.5$ and $w_{NiO}\% = 15\ \%$, ρ_{cat} becomes 2335 kg m^{-3}, close to that in Ref. [52]. The Ni surface area of Ni/γ-Al_2O_3 catalyst was reported to be 4.1 $m^2\ g^{-1}$ for the catalyst with a metal content of 15.2%, and 3.6 $m^2\ g^{-1}$ for the catalyst with a metal content of 8.7%. In our experiments, Ni content for washcoated catalyst can be more than 20%. The range of Ni surface area of 0.44–8.75 $m^2\ g^{-1}$ in the simulation allows an extensive investigation on the effect of catalyst loading. The thermal conductivity of porous washcoat was calculated from Eq. (5) where k_s, the thermal conductivity of the solid phase, was 6.5 W $m^{-1}\ K^{-1}$ for γ-Al_2O_3. The permeability of porous washcoat could be estimated from washcoat structure, such as using empirical correlation for granular media [41]. Since the actual washcoat structure may be complex, the correlations are far from being precise. Therefore, we pre-set the permeability in simulation. The default value of 10^{-16} m^2 leads to impermeable porous media.

Model implementation and solution scheme

The governing equations of the mathematical model were discretized by structured meshes to be implemented in the commercial CFD software FLUENT 6.3. In meshing, we refined the grids near the interfaces (between free fluid and catalytic washcoat, and between catalytic washcoat and solid wall) in order to capture sharp velocity, temperature and concentration gradients. This is crucial for good convergence. Also the 2nd-order upwind discrete scheme was adopted for momentum, energy, and mass conservation equations to reduce the discrete error. For the structural unit model, the number of mesh elements ranged from 29,985 to 53,585 depending on the washcoat thickness and channel height. Mesh grids for the reduced model were approximately half of that for the structural unit model. Refining the mesh did not cause significant change in results.

The discretized equations were solved numerically by FLUENT, whose solver handles the governing equations of fluid transport. Whereas, an in-house C-based stiff ODE solver computes the chemical source terms. The porous media model in FLUENT was enabled to deal with the momentum and heat transfer problems in the catalytic washcoat. The effective diffusivity $D_{i,eff}$ in the catalytic washcoat was calculated by means of the user-defined functions (UDFs) provided by FLUENT. For calculation of the velocity field within the catalytic washcoat, we chose the default superficial velocity $\mathbf{u}_{su}$ from the porous media model offered by FLUENT instead of the physical velocity $\mathbf{u}_{phy}$. The two velocities are correlated by porosity as

$$\mathbf{u}_{su} = \varepsilon\mathbf{u}_{phy} \quad (17)$$

Although using physical velocity takes into account the velocity increase in the porous media relative to the free fluid region, it causes convergence difficulty because the continuity of velocity is preserved across the free fluid porous media interface. Since the actual velocity in porous media was rather small, using superficial velocity is a cost-effective option that would not cause significant accuracy loss.

The proposed solution scheme for FLUENT implementation of the mathematical model is as follows: FLUENT first

Please cite this article in press as: Cao C, et al., Numerical analysis on steam methane reforming in a plate microchannel reactor: Effect of washcoat properties, International Journal of Hydrogen Energy (2016), http://dx.doi.org/10.1016/j.ijhydene.2016.09.034

solves for the velocity, temperature and concentration fields in the computational domains; the information is whereafter past to the in-house stiff ODE solver through UDFs as initial conditions; the stiff ODE solver iteratively solves the set of kinetic equations using a semi-implicit discrete method [54]; the obtained chemical source terms are then returned to FLUENT through UDFs to update the flow field. This process continues until the solution is convergent. The convergence criteria are: The residuals of all governing equations are below 10^{-6}; the velocity, temperature, and concentration fields remain unchanged between two iterations (relative difference < 0.1%).

Results and discussion

Model validation

The washcoat-resolved CFD model was validated against our previous experimental data [39]. In the experiments catalyst substrates were coated with three catalyst loadings (defined as weight of the coated catalyst per substrate area), namely, 6.8 g/m^2, 3.4 g/m^2, and 1.6 g/m^2. For the 6.8 g/m^2 catalyst loading, the Ni content was 15.2%. The corresponding Ni surface area was set to 4.1 m^2 g^{-1} in simulation [55]. For the 3.4 g/m^2 and 1.6 g/m^2 loadings, Ni surface areas were set proportional to their loadings as 2.05 m^2 g^{-1} and 1.03 m^2 g^{-1}, respectively.

As shown in Fig. 2, the simulation results in this work agree well with the experimental data. The simulated CH_4 conversions and CO_2 selectivities for the 6.8-g/m^2 loading quantitatively coincide with experimental data within a wide range of temperature and space velocity. Simulations for the other two loadings also reproduce conversion trends in accord with the experiments. Nonetheless, catalyst activity appears somewhat underestimated in the simulation for the 3.4-g/m^2 loading, especially at high space velocities, while the predicted catalyst activity for the 1.6-g/m^2 loading is slightly higher at low temperatures. These deviations are most probably due to the inaccurate Ni surface areas used as we assumed the linear relationships between catalyst loading and metal surface area. It has been reported that the 8.7 wt% Ni catalyst has a metal surface area of 3.6 m^2/g, which is close to 4.1 m^2/g of the 15.2 wt% catalyst [56]. It is probable that the real Ni surface area of the 3.4-g/m^2 loading catalyst is greater than 2.05 m^2 g^{-1}, while the Ni surface area of the 1.6-g/m^2 loading catalyst is less than 1.03 m^2 g^{-1}. Better agreement with experiment can be obtained by using more appropriate metal surface area. Correlating the metal surface area with factors such as the metal content, the support structure, and the preparation method, etc. is however beyond the scope of this study. Overall, catalytic reaction and the simultaneous mass transfer within the washcoat are properly described by the proposed modeling scheme.

It should be noted that the results generated by our previous model [37], as indicated by the dashed lines, are also consistent with experiments. However, the newly proposed model here has taken account of washcoat with finite thickness; it does not rely on the empirical Surface Area Factor (SAF, ratio of active catalytic surface area to the geometrical area), which requires fitting to experiments, as used in the previous work. Instead, the total active catalytic surface area was calculated from the physical properties of the catalyst (Eq. (16)) without any additional fitting.

In addition, the heat-transfer sub-model included in the modeling scheme has been validated in Ref. [36], in which it was coupled with SMR over Rh. In this sense, we are confident that the developed model in the present work is reliable for investigating the effect of washcoat properties for an integrated microchannel reactor running SMR over Ni.

Basic flow, temperature and concentration fields

We first investigated the basic flow, temperature and concentration fields in the catalytic washcoat and free fluid region inside the reforming channel. The results were based on the reduced channel model with a channel height of 0.8 mm under the baseline operating condition (u_{in} = 0.887 m/s, T_w = 1173 K) with the catalyst loading of 6.8 g/m^2.

Fig. 3a depicts the contours of axial velocity component (the transverse velocity component was found to be too small to have visible effects) for washcoat thickness of 25 μm and 100 μm, representing normal and thick washcoat, respectively. For both washcoat thickness, bulk gaseous flows are close to laminar. The axial velocity develops along the channel due to a net species generation (of a factor > 3) from SMR until the end, indicating that the full length of the reactor is utilized. In the porous washcoat, however, the velocities are small (in the order of 10^{-3} m/s) and resemble plug flows. The flow pattern with such impermeable washcoat ($\kappa = 10^{-16}$ m^2) indicates that the reactants flow by rather than through the catalyst, in accord with Tonkovich et al. [10]. Hence, thicker washcoat is equivalent to smaller cross-sectional area, and results in greater average velocity in the open gap of the channel (free fluid region). As can be seen, the maximum outlet velocity for the thick washcoat (2.47 m/s) is larger than the normal washcoat (2.03 m/s), although the net species generation for the former is less because of its lower CH_4 conversion. Therefore, the residence time of gaseous species is largely influenced by washcoat thickness at fixed volumetric flow rate.

Fig. 3b and c shows the axial velocity profiles in the transverse direction at x = 22.5 mm (in the middle of the channel). The axial velocity distributions are different, especially at the interface, with permeability ranging from 10^{-8} to 10^{-16} m^2. For the permeability of 10^{-8} m^2, the washcoat appears fully permeable, marked by the smooth transition of axial velocity at the interface. When the permeability is less than 10^{-12} m^2, the axial velocity distributions are almost indistinguishable. The washcoat is impermeable except for the region very close to the interface. In that transition area, velocity gradient exists which decreases with permeability (see the zoomed-in parts). Even though the washcoat permeability has significant effect on the velocity distribution, it hardly changes the CH_4 conversion (<0.8%) regardless of washcoat thickness. It suggests that convective mass transfer is trivial compared with diffusion within the catalytic washcoat. In addition, we estimated the permeability of catalytic washcoat in experiments using empirical correlation for granular media [41], which resulted in no more than 10^{-14} m^2.

Please cite this article in press as: Cao C, et al., Numerical analysis on steam methane reforming in a plate microchannel reactor: Effect of washcoat properties, International Journal of Hydrogen Energy (2016), http://dx.doi.org/10.1016/j.ijhydene.2016.09.034

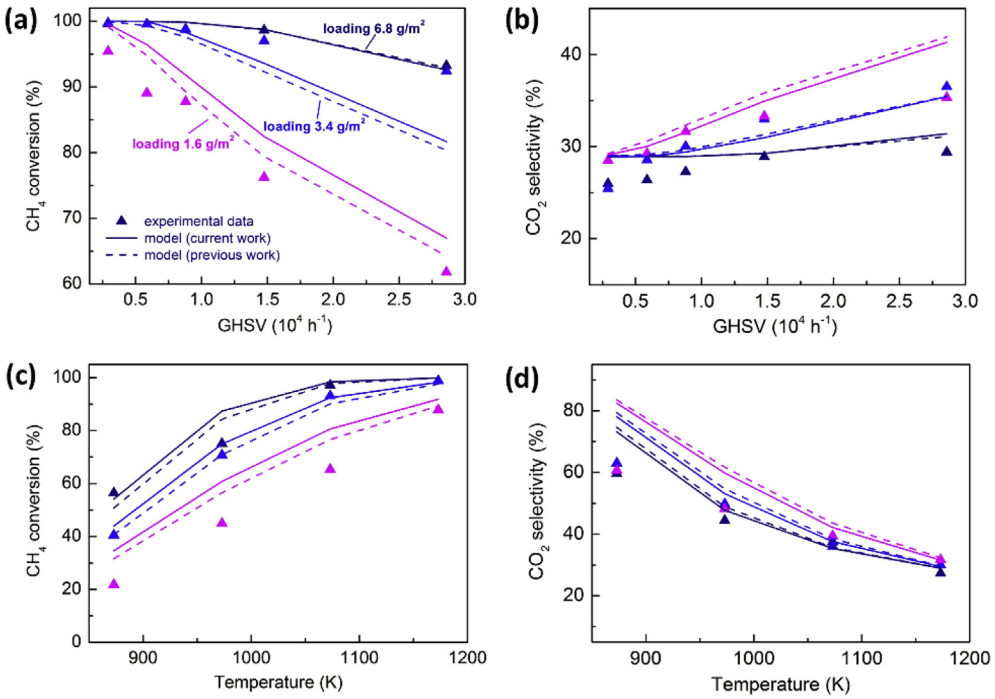

Fig. 2 – Comparison of simulated and experimental results of CH_4 conversion and CO_2 selectivity for (a) and (b): $T_w = 1173$ K, GHSV $= (0.29–2.86) \times 10^4$ h^{-1}; (c) and (d): $T_w = 873–1173$ K, GHSV $= 0.88 \times 10^4$ h^{-1}. In all cases, $H_r = 0.4$ mm and $T_{in} = T_w$.

It implies that impermeable porous media is a good approximation for the catalytic washcoat. Consequently, the permeability of 10^{-16} m^2 was set as default in the other simulations.

Fig. 4 demonstrates the temperature profile along the centerline of the reforming channel for different inlet temperatures. The temperature in the channel reaches the wall temperature in 5 mm from inlet (dashed line). The corresponding changes in the CH_4 conversion are lower than 0.3%. The temperature curves for the case of 25-μm washcoat overlap with that for the 100-μm washcoat (not shown for clarity), indicating the microchannel reactor has the same heat transfer capability with the 100-μm washcoat as the 25-μm one. Under the condition of coupled catalytic combustion and reforming, similar rapid heat-up of inlet flow is observed (Fig. 10) which will be discussed with more detail in Section Optimization of catalytic washcoat. This tremendous transverse heat transfer performance guarantees high space velocity operation of the intense endothermic SMR.

Fig. 5 shows the contours of the mass fractions of CH_4, H_2O, H_2, CO and CO_2 for the 100-μm washcoat. For all species, the transverse gradients in the open gap are insignificant compared with those in the catalytic washcoat, indicating much more intense diffusive resistance in the porous media region than in the gas phase. These trends are also observed with 25-μm washcoat though less obvious (not shown). On reactant side, CH_4 mass fraction is non-zero throughout the washcoat in the anterior part of channel ($x < 0.02$ m) as shown in Fig. 5a. All active sites of the catalyst are accessible in this region even for this thick washcoat. However, the gradient increases towards the end of the reactor. In the end of the channel, the active sites at the bottom of washcoat cannot be accessed by CH_4. The excessive reactant H_2O behaves differently from CH_4. Owing to its abundance, the mass fraction of H_2O is no less than 0.45 over all active sites in the entire channel (Fig. 5b). The resulting H_2O conversion does not vary with washcoat thickness much. Yet the mass fraction gradient close to the inlet is apparently larger than CH_4, implying somehow faster consumption of H_2O in this region.

On the product side, Fig. 5c and d shows that the mass fractions of H_2 and CO exhibit similar tendencies. They distribute everywhere in the washcoat, but H_2 has smaller transverse gradients compared with CO, as indicative of the faster diffusion due to its low molecular weight ($M_{H_2} = 2 \times 10^3$ kg/mol). However, Fig. 6e indicates that the mass fraction of CO_2, the heaviest product ($M_{CO_2} = 44 \times 10^{-3}$ kg/mol), does not vary notably across the washcoat. Also, the formation of CO_2 is completed within the first 0.01 m of the channel, and the gradient of mass fraction within washcoat is only observed at the inlet region ($x < 0.01$ m). A remarkable difference found among the products is that CO generates more slowly than the other two, as inferred from its greater axial gradients. It is clear the formation of products is not simultaneous but rather follows different reaction paths.

The intense CO_2 formation near the inlet suggests the existence of massive O(s) (surface adsorbed oxygen), which further oxidizes CO(s) into CO_2(s) through reaction R21 in Table A.1. As O(s) originates from the decomposition of H_2O(s), the region featuring more CO_2 formation also features faster H_2O decomposition (reaction R16 in Table A.1), which produces more H_2 (through reactions R16 and R7 in Table A.1). This in turn explains the above-mentioned larger gradient of the mass fraction of H_2O within washcoat in the inlet region. With the growth of H_2 along the channel, coverage of H(s) increases resulted from the adsorption/desorption equilibrium. H(s) suppresses the decomposition of H_2O and finally

Please cite this article in press as: Cao C, et al., Numerical analysis on steam methane reforming in a plate microchannel reactor: Effect of washcoat properties, International Journal of Hydrogen Energy (2016), http://dx.doi.org/10.1016/j.ijhydene.2016.09.034

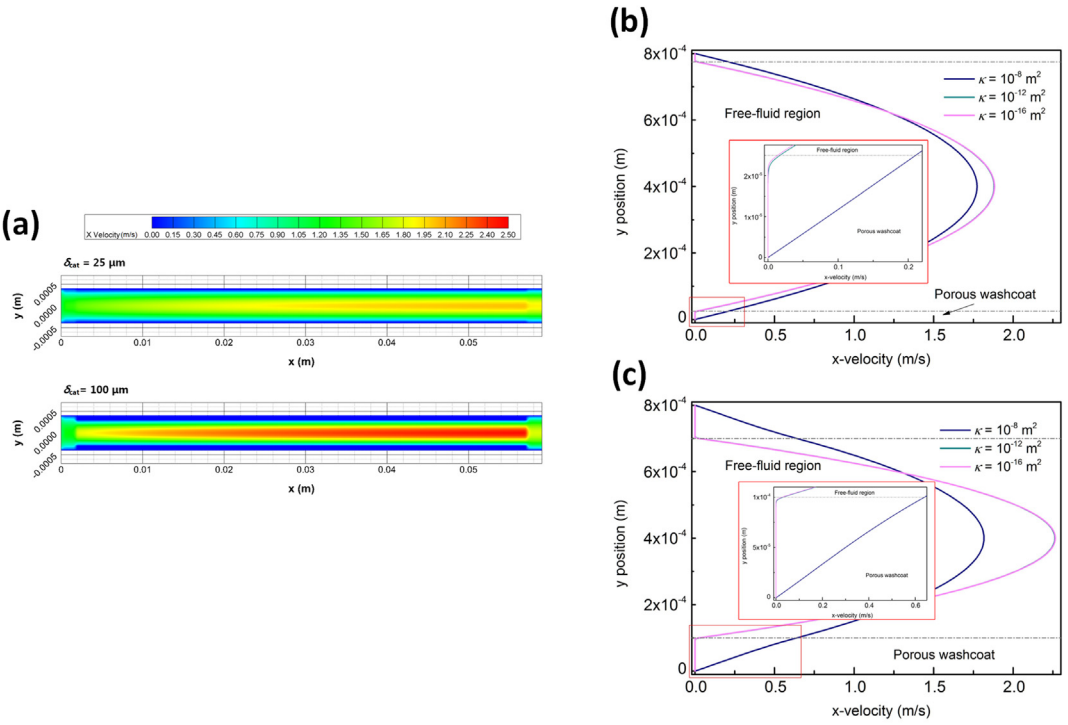

Fig. 3 – (a) Contours of axial velocity in the reforming channel; transverse axial velocity profiles at $x = 22.5$ mm for (b) 25-μm washcoat and (c) 100-μm washcoat with different permeabilities.

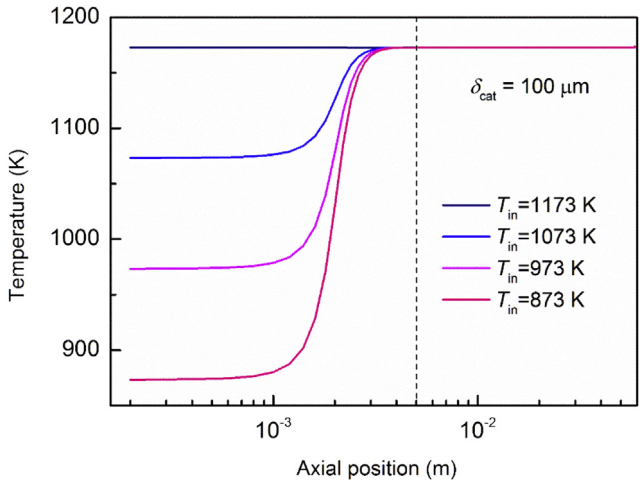

Fig. 4 – Temperature profiles along the centerline of the reforming channel with $\delta_{cat} = 100$ μm.

the oxidation of CO(s), so that CO_2 is seldom formed in the remaining channel. From a macroscopic view, H_2 is generated by both SMR and WGS close to the inlet, but mostly by SMR alone in the rest of the channel. The obtained knowledge of catalyst usage and dominant reactions under the baseline condition provides the clue to analyze the reactor performance under various theoretical and practical conditions.

Basics of coupled reaction and internal mass transfer

Although the catalytic washcoat coated on the reactor wall is thin, it has been suggested from the significant concentration gradients that internal mass transfer limitation may be critical for SMR in microchannel reactor. We therefore investigate the basic problem regarding the coupling of surface reaction and mass transfer in the catalytic washcoat, involving the limiting regime of process, catalyst usage for different washcoat dimension (thickness), and the possible effect of washcoat structure on reactor performance. These aspects regarding internal mass transfer limitation were explored by simulations concerning the reforming channel and reforming catalyst within the reduced model geometry under the assumption of constant wall temperature.

The limiting regime of the process can be verified by varying the washcoat dimension with other parameters fixed. The reactant conversions and product yields and selectivity were explored at 1173 K and 1073 K, which represent high and low operating temperatures, respectively. In each set of simulation, the washcoat thickness was varied from 10 μm to 100 μm with the overall catalyst loading fixed, while GHSV was kept as 1.48×10^4 h^{-1} all along. Fig. 6a shows that the CH_4 conversion decreases linearly with increasing washcoat thickness for all three loadings and both temperatures. As demonstrated, the CH_4 conversion is not equilibrium-limited; hence, the figure shows evident effect of internal mass transfer. It is also noted that the H_2 yield decreases with increasing washcoat thickness following the CH_4 conversion (not shown). On the other hand, decreasing the catalyst loading from 9.1 g/m^2 to 4.5 g/m^2 leads to a decrease of the CH_4 conversion up to 10%, which is comparable to that caused by increasing washcoat thickness from 10 μm to 100 μm. The reactor thereby appears to run in a mixed limiting regime of reaction and internal mass transfer.

The H_2O conversion in Fig. 6b does not vary significantly with washcoat thickness. The difference between H_2O and

Please cite this article in press as: Cao C, et al., Numerical analysis on steam methane reforming in a plate microchannel reactor: Effect of washcoat properties, International Journal of Hydrogen Energy (2016), http://dx.doi.org/10.1016/j.ijhydene.2016.09.034

CH_4 is not likely due to diffusion in that they have similar diffusivity. On one hand, the conversion trend can be attributed to the fact that H_2O is largely excessive: Under S/C = 3, H_2O conversion is 1/3 of CH_4 conversion if water-gas shift is ignored. On the other hand, it is probable that the consumption of H_2O is more reaction-controlled, because the adsorption and decomposition of H_2O over Ni surface (reactions R9, R16 and R18 in Table A.1) tend to be slower than that of CH_4

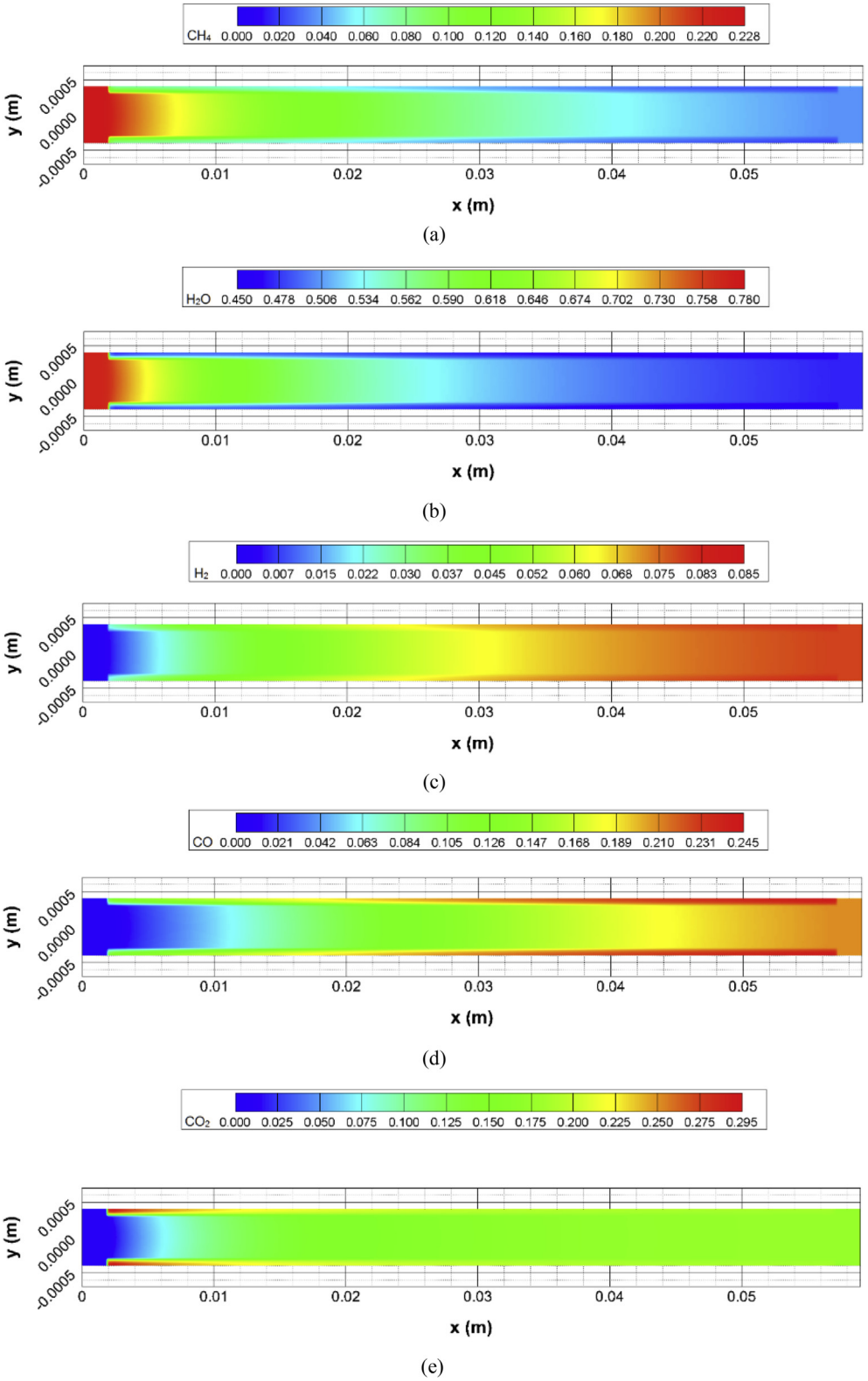

Fig. 5 – Contours of species mass fractions of (a) CH_4 (b) H_2O (c) H_2 (d) CO and (e) CO_2 in the reforming channel with $\delta_{cat} = 100$ μm.

Please cite this article in press as: Cao C, et al., Numerical analysis on steam methane reforming in a plate microchannel reactor: Effect of washcoat properties, International Journal of Hydrogen Energy (2016), http://dx.doi.org/10.1016/j.ijhydene.2016.09.034

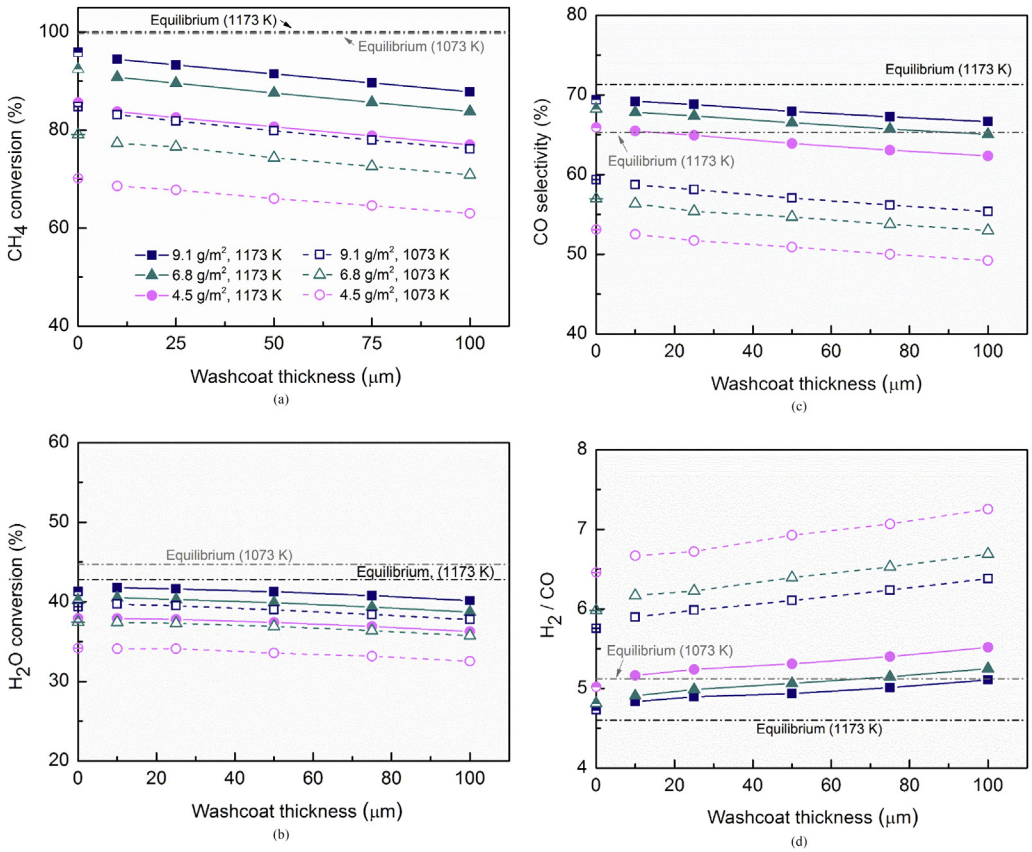

Fig. 6 – (a) CH_4 conversion, (b) H_2O conversion, (c) CO selectivity, and (d) H_2/CO molar ratio at different washcoat thickness with overall catalyst loading (weight of coated catalyst per unit substrate area) fixed.

(reactions R12, R23 and R31 in Table A.1) concerning the corresponding reaction barrier heights.

In Fig. 6c, the CO selectivity (defined as $\frac{n(CO)}{n(CO)+n(CO_2)}$) decreases with increasing washcoat thickness. This trend probably arises from the kinetics of SMR over Ni that CO_2 forms prior to CO as discussed before. As CH_4 conversion decreases with increasing washcoat thickness, incomplete CO formation leads to lower CO selectivity. Fig. 6d demonstrates that the molar ratio of H_2 to CO increases with washcoat thickness. The increasing trend of H_2/CO indicates that the decrease of the CO selectivity (and thus the CO yield) outweighs the decrease of the H_2 yield, possibly as a result that the decrease of the H_2 yield can be partially compensated by WGS, which is not weakened that much by the thick washcoat due to the abundance of H_2O.

To confirm the limiting regime at which the reactor is operated, we plotted the Damköhler number (*Da*) profiles on CH_4 and H_2O basis in Fig. 7 for different washcoat thicknesses. The definition of *Da* used for catalyst with slab geometry was

$$Da = \frac{R_i(y = \delta_{cat})\delta_{cat}^2}{C_i(y = \delta_{cat})D_{eff}} \quad (18)$$

Fig. 7a and b shows that *Da* increases with washcoat thickness, as indicative of the ever-stronger process limitation by internal mass transfer. Fig. 7a indicates that *Da* on CH_4 basis remains in the range of 10^{-1}–10^{1} all along the channel with washcoat thickness in the range of 10–100 μm. The situation is similar at 1073 K or with other loadings (not shown for brevity). That is to say, the surface reaction and mass transfer for CH_4 have comparable rates; therefore, they are strongly coupled. Thus, it is verified that the process is in a mixed limiting regime. *Da* on H_2O basis as shown in Fig. 7b mostly stays below unity, indicating a more reaction controlled regime for H_2O. It justifies the second reasons proposed before why the H_2O conversion remains roughly constant with varying washcoat thickness (Fig. 6b).

When comparing the dependence of CH_4 conversion on washcoat thickness in this work (Fig. 8a) with that of Stutz and Poulikakos [14], we found remarkable similarities. They showed that for partial oxidation of CH_4 over Rh in monolithic reactor, the CH_4 conversion also decreases monotonically and almost linearly with washcoat thickness (although with greater magnitude) if the inlet velocity remains constant. Given that Rh-based SMR is reaction-controlled in microdevices [57], the Ni-based process seems undoubtedly reaction limited owing to the relatively lower catalytic performance of Ni. Preliminary analysis on relevant time scales of transport and reaction indicates that the characteristic time of internal mass transfer is 1–2 orders of magnitude smaller than that of surface reaction. However, washcoat thickness, despite its small dimension, shows a significant effect on the reactor performance for Ni-based SMR. To clarify the mode of the reaction-diffusion interplay, we analyzed the spatial distribution of effectiveness factor along the channel. As shown in

Please cite this article in press as: Cao C, et al., Numerical analysis on steam methane reforming in a plate microchannel reactor: Effect of washcoat properties, International Journal of Hydrogen Energy (2016), http://dx.doi.org/10.1016/j.ijhydene.2016.09.034

Fig. 8a, the effectiveness factor profile on CH_4 basis rises drastically close to the entrance, forming a developing region, but then quickly flattens out. Within the ~5 mm developing region, the effectiveness factor increases with decreasing washcoat thickness and shows no convergence trend. Near the outlet, the effectiveness factor is approximately fully developed and approaches unity for the thin washcoat. The pattern of effectiveness factor profile implies high initial rates of surface reaction that overwhelms the rate of mass transfer within the thin washcoat. The high initial rate, which is intrinsic in the kinetics of SMR, is strengthened in microchannel reactor due to its high space velocity and large catalyst loading. Hence higher reactor throughput eventually leads to more strongly coupled reaction-diffusion and thus inevitable internal diffusional limitation. With this respect, the dimension of catalytic washcoat has to be optimized to avoid unnecessary loss of catalyst productivity due to internal diffusion for SMR over Ni in microchannel reactor.

For completeness, the effectiveness factor profile on H_2O basis is shown in Fig. 8b as the counterpart of Fig. 8a. It is obvious that the distribution is substantially different from that on CH_4 basis. Thinner washcoat corresponds to larger effectiveness factors at the channel inlet, and the effectiveness factor starts to grow along the channel. At $x = 27.6$ mm, the effectiveness factor of the thinnest washcoat (10-μm) is exceeded by the 25-μm washcoat, which is again exceeded by the 50-μm washcoat at $x = 47.5$ mm. Although the thickest washcoat (100-μm) holds the lowest effectiveness factor all along the channel, it seems to be an issue of the restricted channel length: with sufficiently long reaction channel, the effectiveness factor of the 100-μm washcoat would undoubtedly exceed all those of the thinner washcoats. Another remarkable feature is that the effectiveness factor on H_2O basis can exceed unity – a feature more obvious for the thicker washcoat. It suggests that the surface reaction consuming H_2O inside the washcoat becomes faster than at the interface in the posterior part of reactor. It can be attributed to the fact that at specific point of the reactor the water-gas shift reaction changes its direction (from positive to negative), which happens outside-in the catalyst bed [52]. Also noted is that in comparison with global kinetics models, the use of microkinetics herein avoids the negative or asymptotic values of effectiveness factor [52,58–61], which are counter-intuitive. In contrast, the effectiveness factors in this work correspond to net consumption of CH_4 and H_2O over catalyst surface, that is, the difference between adsorption and desorption rates, thus providing a clear and realistic scheme of the complex transport-reaction phenomena at washcoat scale. Although the effectiveness factor on H_2O basis is not related to reactor performance herein due to high S/C, it would be intriguing to extend the investigation to lower S/C ratios (e.g., <2), at which new characteristics may araise.

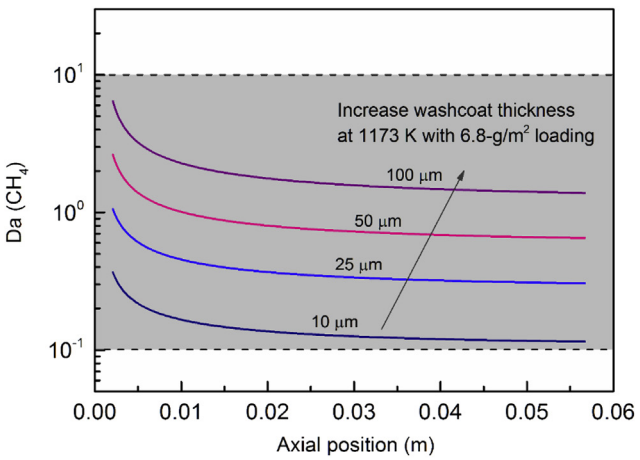

Fig. 7 – Damköhler number along the reaction channel on (a) CH_4 and (b) H_2O basis at 1173 K with overall catalyst loading of 6.8 g/m².

Fig. 8c illustrates the overall catalyst usage as a function of washcoat thickness. The overall catalyst usage, $\overline{\eta}$, was defined as a characterization of the "efficiency" active sites usage in the whole catalyst bed,

$$\overline{\eta} = \frac{\text{reactant actually converted in catalyst bed}}{\text{reactant converted without internal diffusion}} = \frac{1}{L}\int_0^L \eta(x)dx \tag{19}$$

where the effectiveness factor η corresponding to catalyst slabs was:

$$\eta = \frac{\text{apparent reaction rate}}{\text{intrinsic reaction rate}} = \frac{\int_0^{\delta_{cat}} R_i(y)dy}{\delta_{cat} R_i(y=\delta_{cat})} \tag{20}$$

It is clear that the catalyst usage monotonically increases with decreasing washcoat thickness, and there is no trend for the increase to slow down until 100% usage. With increased catalyst loading and temperature, the catalyst usage decreases due to the faster surface reaction that competes with internal mass transfer. Nonetheless, with a normal washcoat thickness around 25 μm, the catalyst usage is over 80% regardless of loading and temperature. In comparison, the industrial Ni-based catalyst used in fixed-beds has orders of magnitudes lower effectiveness factor, which is usually set in the range of 0.001–0.1 in simulation [62–66]. Thus, the simulation proves that thin catalytic washcoat in microchannel reactor can lead to immense improvement of catalyst usage

Please cite this article in press as: Cao C, et al., Numerical analysis on steam methane reforming in a plate microchannel reactor: Effect of washcoat properties, International Journal of Hydrogen Energy (2016), http://dx.doi.org/10.1016/j.ijhydene.2016.09.034

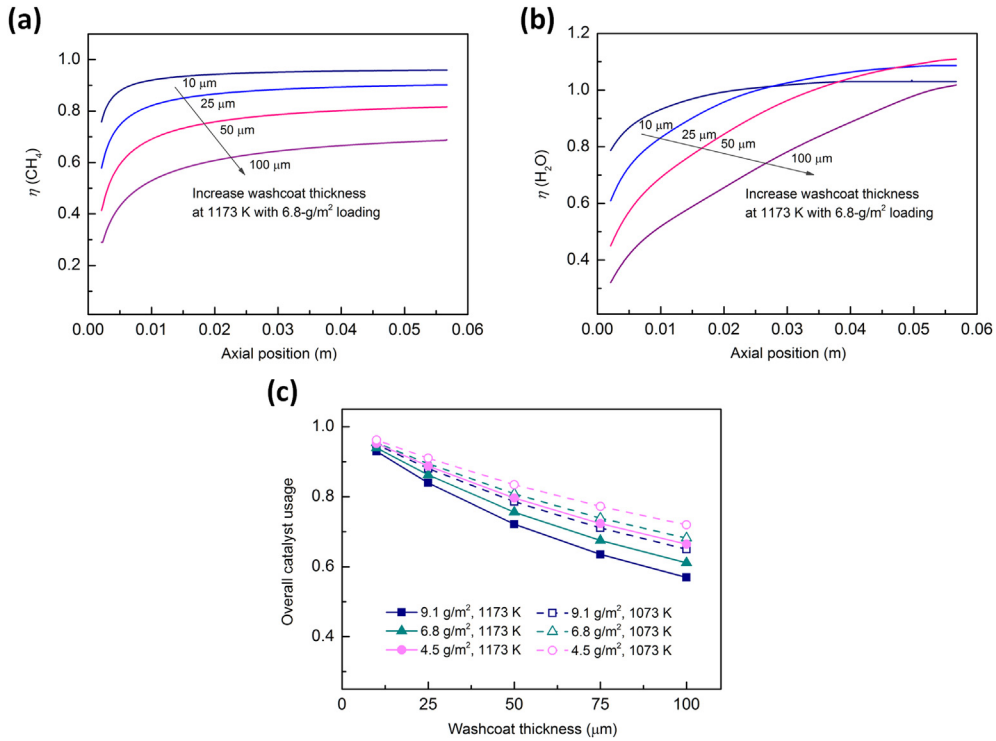

Fig. 8 – Effectiveness factor profiles along the reaction channel on (a) CH_4 and (b) H_2O basis for different washcoat thickness with overall catalyst loading of 6.8 g/m^2; (c) overall catalyst usage on CH_4 basis as a function of washcoat thickness.

compared with the catalyst in the form of shaped extrudates due to effective reduction of intra-particle temperature and concentration gradients.

Optimization of catalytic washcoat

The practical implication of optimizing the catalytic washcoat is drawn from the detailed reaction and mass transfer coupling within the catalytic washcoat revealed by the washcoat-resolved CFD model. By tuning the washcoat properties, we are able to trade off among stable operation, high reactor throughput and catalyst productivity, etc. in process development to fulfill various specific demands. In the sub-sections below, we are to discuss two most basic and important aspects of the washcoat properties, i.e., washcoat structure and washcoat dimension (thickness).

Washcoat structure

Since SMR in microchannel reactor is limited by reaction and internal mass transfer, the reactor performance is expected to be significantly affected by the effective diffusivity of the washcoat. Effective diffusion within washcoat is the combination of molecular diffusion, which occurs in macropores, and Knudsen diffusion, which governs the mass transport in micropores. Therefore the textural properties of catalyst support, e.g., pore size, porosity, tortuosity, etc., dominate the effective diffusivity (see Eq. (6)). It is then of great interest to conduct a parametric study on the impact of the support structure on reactor performance. We varied the pore diameter and porosity in the simulations with the single channel model at constant wall temperature of 1173 K and with a washcoat thickness of 25 μm. Fig. 9a and b shows the respective species concentration profiles corresponding to varying the pore diameter and porosity with other parameters fixed. With a typical washcoat porosity of 0.5, increasing pore diameter improves CH_4 and H_2O conversions and H_2 and CO yields (Fig. 9a). The CO_2 yield, however, remains unaffected by the pore diameter, although larger pores do lead to more rapid formation of CO_2 in the anterior part of the reactor. We also notice that the slope (absolute value) of the concentration curve increases with the pore diameter especially near the reactor inlet, indicating the notably higher initial reaction rates enabled by the larger pores. However, the improvement of the overall reactor performance is less significant when the pore diameter is increased from 8 nm to 50 nm than from 2.5 nm to 50 nm.

The sensible response of species concentration profiles to the pore diameter is consistent with the fact that Knudsen diffusivity is ~2 orders of magnitude smaller than molecular diffusivity, which means the small micropore size is the limiting factor of effective diffusion within porous washcoat. The pore size of alumina support is greatly tunable: It could range from the order of 10 nm [53] for the catalytic washcoat in monolith, to the order of 300 nm [52] for the industrial catalyst used in fixed-beds. By contrast, the limit of porosity on effective diffusion is much weaker, given that the porosity never exceeds 1 and the typical value is around 0.5. This is in accord with Fig. 9b in which the porosity shows little impact on the species profiles with a pore diameter of 20 nm. In all, the simulation results suggest to increase the fraction of

Please cite this article in press as: Cao C, et al., Numerical analysis on steam methane reforming in a plate microchannel reactor: Effect of washcoat properties, International Journal of Hydrogen Energy (2016), http://dx.doi.org/10.1016/j.ijhydene.2016.09.034

macropores rather than the total pore volume for better effective diffusion within the catalytic washcoat.

The other vital impact of the washcoat structure is that it possibly plays a role in the thermal management of microchannel reactor. It is a well-known advantage of microchannel reactor for highly endothermic SMR that on-site catalytic combustion can be integrated. For catalytic combustion assisted SMR in microchannel reactor, co-current configuration (sketched in Fig. 1a) is preferred to counter-current or cross-current configuration in light of the more even temperature field within and between reforming channels [67]. This better temperature distribution is resulted from the good overlap of corresponding reaction zones, that is, the synchronized rates of catalytic combustion and SMR in the anterior part of the reactor. However, bearing in mind that catalytic combustion is a very fast reaction relative to SMR, the Ni-based process has inherently poorer heat match due to slower reforming kinetics than the Rh-based one. The undesired mismatch could be even worse when the apparent reforming rate is further limited by internal mass transfer, leading to possible hotspot formation. This issue with regard to reactor thermal management necessitates the optimization of washcoat accounting for the coupled reaction, mass transfer, and heat transfer.

We investigated the temperature profiles of the reforming channel under the catalytic-combustion assisted condition using the structural unit model, taking into account several combinations of washcoat thickness and pore diameter with the reference to the case of instantaneous diffusion (neglecting internal mass transfer limitation). CH_4 was used as the combustion fuel, which was pre-mixed with stoichiometric O_2 and balanced N_2, and the fuel to reform gas molar ratio was 1:3.5. As shown in Fig. 10, the temperature of the reforming channel increases with washcoat thickness with the fixed pore diameter of 20 nm and catalyst loading of 9.1 g/m^2. The hotspot temperature with the thickest washcoat (100 μm) is 46 K higher than the hypothetical condition of instantaneous diffusion. However, this high temperature does not benefit CH_4 conversion: a higher CH_4 conversion (94.1%) is obtained with the 25 μm washcoat, which corresponds to lower temperature close to the condition of instantaneous diffusion. In brief, longer diffusion length reduces the mass transfer rate and thus the apparent reaction rate, causing remarkable temperature rise, which however cannot offset the reaction rate loss in return if the washcoat is as thick as 100 μm.

The temperature curve for the pore diameter of 2.5 nm, which represents smaller effective diffusivity of washcoat, has both the highest peak temperature and the greatest temperature difference along the channel compared with all the others. In this case, the CH_4 conversion is also considerably low while the H_2/CO ratio is close to other cases. The specific shape of the temperature curve corresponding to small effective diffusivity can be explained by a slower initial apparent reforming rate and higher apparent rate at the later stage, in accord with the form of concentration profile for the small pore diameter demonstrated in Fig. 9a. It is clearly suggested that washcoat with a small pore diameter is unfavorable regarding productivity and materials and catalyst stability because of the low CH_4 conversion and high temperature difference.

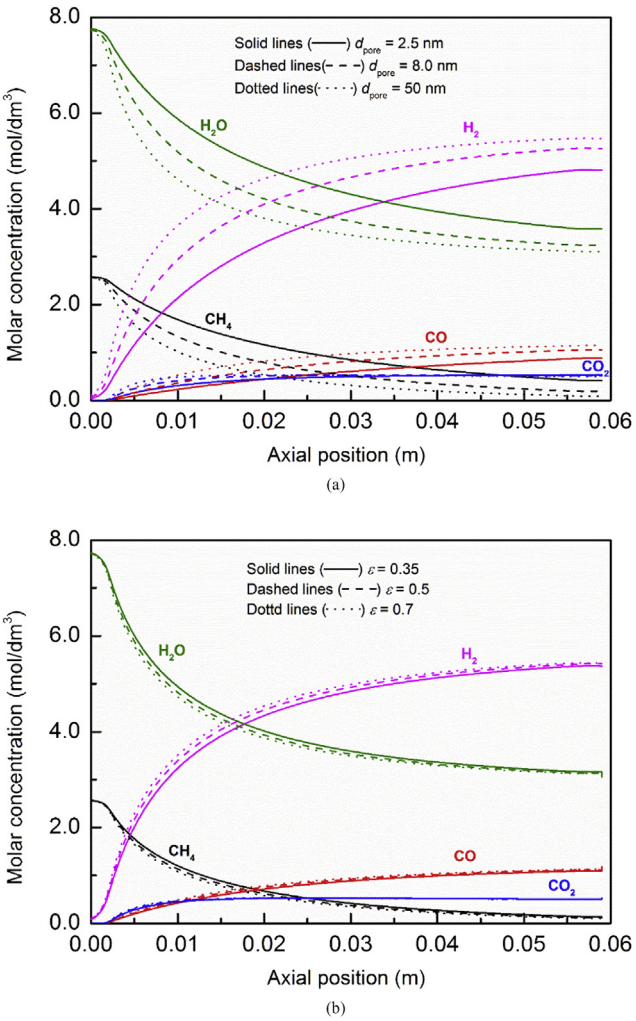

Fig. 9 – Species concentration profiles for different (a) pore diameters and (b) porosities. In (a) the porosity was 0.5 while in (b) the pore diameter was 20 nm.

It is important to note that in the simulation the non-optimal combustion catalyst loading and fuel flow rate, as well as the relatively high inlet temperatures (1173 K) all amplify the temperature difference within the reactor leading to higher hotspot temperature. Therefore, former discussions are not quantitative indication but rather general trends, which highlighted the importance of providing sufficiently high effective diffusivity and limited dimension for washcoat so as to achieve better reactor temperature control and thermal management.

Washcoat thickness

The pursuit for a high reactor throughput, which is especially crucial for microchannel reactor, can be achieved primarily by increasing the catalyst productivity. In practice, volumetric catalyst productivity can be improved via two routes: increasing the volumetric loading of active Ni within a given catalyst support, and increasing the active surface area provided by the Ni particles. Although enlarging volumetric loading or reducing crystal size (for larger superficial area) is

Please cite this article in press as: Cao C, et al., Numerical analysis on steam methane reforming in a plate microchannel reactor: Effect of washcoat properties, International Journal of Hydrogen Energy (2016), http://dx.doi.org/10.1016/j.ijhydene.2016.09.034

not severely limited by the textural properties of catalyst support and metal particles, in consideration of long-period catalyst stability, substantially large volumetric loading or undersized metal crystal may lead to high risk of sintering and leaking, which cause catalyst deactivation. Hence, catalyst productivity is limited after volumetric loading and active metal surface area have been maximized through optimization of catalyst preparation.

What remains to increase the throughput of microchannel reactor with plate-type structured catalyst is to washcoat thicker catalyst – thus carrying more active phase – on the substrate, to increase the overall catalyst loading. Using thicker washcoat that contains proportionally more active sites enables to convert additional feedstock, leading to higher reactor throughput. However, the increased volumetric reactor performance comes at the expense of reduced catalyst productivity. As summarized from Fig. 6, longer diffusion length and faster surface reaction lower the catalyst usage owing to internal mass transfer limitation. In addition to those, higher GHSV may also reduce the catalyst usage due to lower residence time for transverse mass transfer to occur. The effect of GHSV on mass transfer within the washcoat is studied with a halved channel height of 0.4 mm. Smaller channel height could reduce the possible confusive impact of GHSV on external mass transfer – It has been shown [21] that with channel heights less than 0.70 mm, the CH_4 conversion remains constant at WHSV up to 2.8×10^3 h^{-1}. For a 25 μm washcoat as shown in Fig. 11, with increasing GHSV, the effectiveness factor reduces visibly at the inlet region, and its profile develops more slowly. The overall catalyst usage at the largest GHSV (corresponds to the residence time of 15 ms) is found ~90% of that at the smallest GHSV (corresponds to the residence time of 104 ms). If the washcoat is thicker, the reduction of effective catalyst usage with increasing GHSV would be even more severe than the presented case.

To clarify the decline of catalyst productivity with increasing washcoat thickness at constant volumetric catalyst loading, we conducted additional simulation with the 0.4 mm channel and the catalyst loading corresponding to 10 wt% of Ni. This volumetric loading was achieved by fixing the active surface area at 2.6 m^2/g, under the assumption of the linear relationship between the active surface area and catalyst loading. Fig. 12 shows the contours of CH_4 conversion with respect to WHSV (based on the weight of catalyst, as an indication of catalyst productivity) and washcoat thickness, where zero washcoat thickness means instantaneous internal diffusion. At any given CH_4 conversion, the WHSV decreases with increasing washcoat thickness up to 75 μm. The descending catalyst productivity with washcoat thickness is more serious at higher WHSVs, as indicated by the steeper contour lines, showing combined effects of longer diffusion length, enhanced total surface reaction, and reduced residence time. With this continuous loss of catalyst productivity,

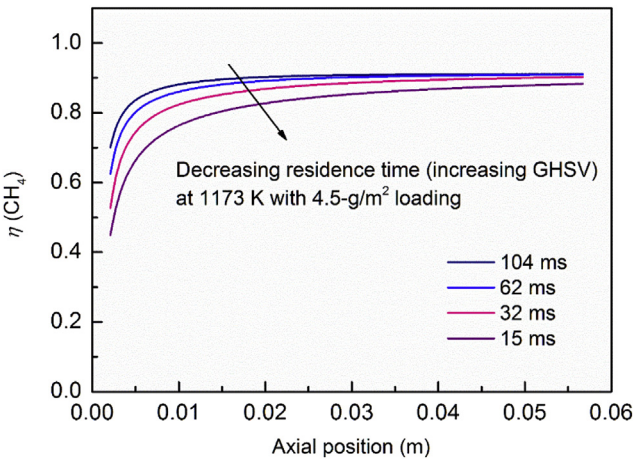

Fig. 11 – Effectiveness factor profiles for different residence times with overall catalyst loading of 4.5 g/m² and $H_r = 0.4$ mm.

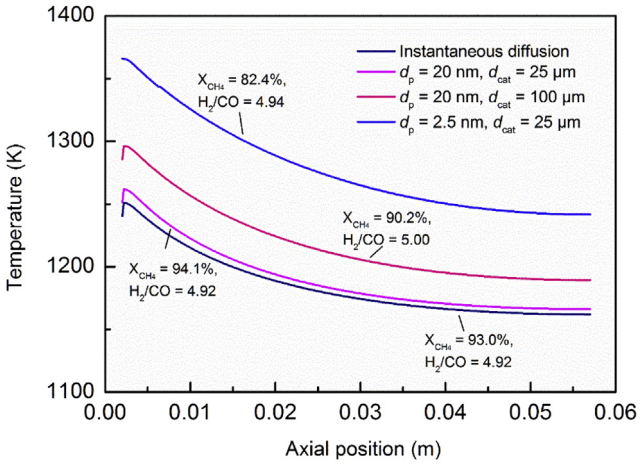

Fig. 10 – Wall temperature of the reforming channel for different washcoat thickness and pore diameters with overall catalyst loading of 9.1 g/m².

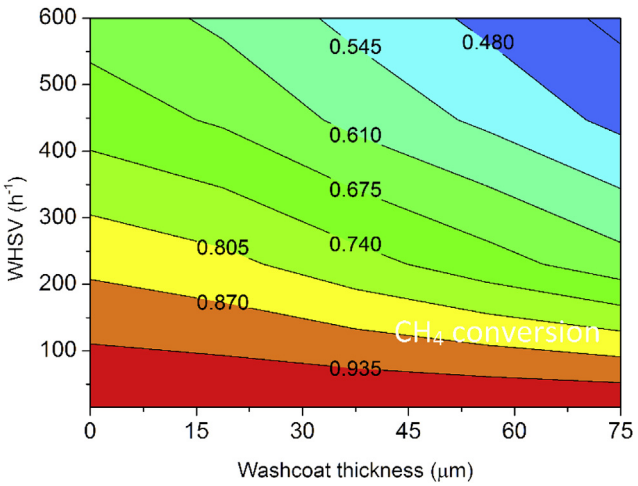

Fig. 12 – Contours of CH_4 conversion with $H_r = 0.4$ mm and Ni content = 10 wt%. X axis indicates washcoat thicknesses and Y axis indicates WHSV. Zero washcoat thickness corresponds to instantaneous diffusion.

Please cite this article in press as: Cao C, et al., Numerical analysis on steam methane reforming in a plate microchannel reactor: Effect of washcoat properties, International Journal of Hydrogen Energy (2016), http://dx.doi.org/10.1016/j.ijhydene.2016.09.034

the reactor throughput can hardly be increased further by coating thicker washcoat, as the extra catalyst is unusable. As a result, the reactor productivity would approach a limit.

Fig. 13 shows the contours of the CH_4 conversion and the H_2/CO ratio in the product with respect to the reactor productivity, as characterized by GHSV, and washcoat thickness, proportional to catalyst loading. Other model parameters used were the same as those in Fig. 12. Fig. 13a demonstrates that the reactor productivity can be well improved by adopting thicker catalytic washcoat with constant volumetric catalyst loading within the upper limit of washcoat thickness of 75 μm in simulation. With the objective of 95.5% CH_4 conversion, the maximum allowed reactor productivity increases from $2.0 \times 10^4\ h^{-1}$ to $3.3 \times 10^4\ h^{-1}$ when the washcoat thickness is increased from 25 μm to 75 μm, which corresponds to increasing catalyst loadings from 6.8 g/m^2 to 20.4 g/m^2. However, the reactor productivity shows a trend to stop the growth beyond 75 μm, as suggested by the decaying catalyst productivity (Fig. 11). Fig. 13b further indicates that the product becomes slightly more H_2-rich when increasing washcoat thickness at specific CH_4 conversion (see points A, B and C). It is the greater diffusivity of H_2 than CO that primarily contributes to the increment, which is preferable for downstream processes of low-CO tolerance. We should add that the volumetric catalyst loading corresponding to 10 wt% used in these presented results is far below the extreme capacity of active Ni metal for porous γ-Al_2O_3 support. Increasing the volumetric catalyst loading is beneficial for the reactor productivity, but is not anticipated to result in a contour distinct from Fig. 13a, that is, the increase in reactor productivity tends to stop beyond 75 μm of washcoat thickness.

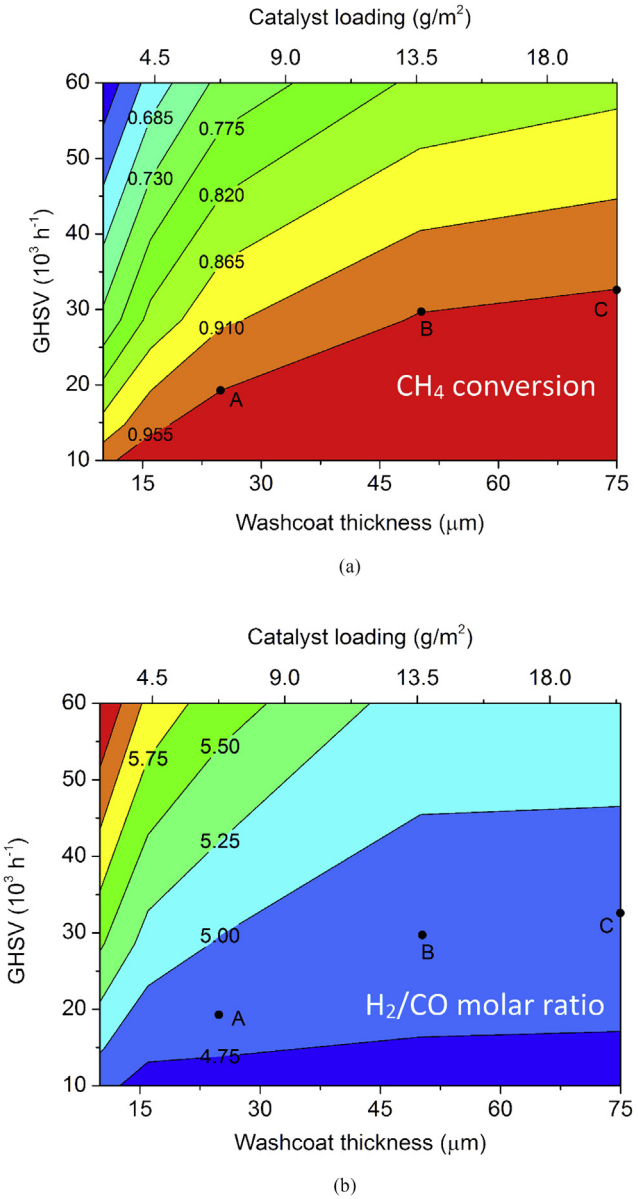

Fig. 13 – Contours of (a) CH_4 conversion and (b) molar ratio of H_2 to CO with $H_r = 0.4$ mm and Ni content = 10 wt%. X axis indicates washcoat thicknesses and Y axis indicates GHSV.

To summarize, optimal washcoat dimension depends on the overall economics balancing the catalyst productivity, reactor productivity and product distribution. Being moderately priced and little in the coated amount, the investment cost of Ni-based catalyst is minor compared with that of bulk materials of microchannel reactor. In such case it is inclined to use a relatively thick washcoat (likely to be up to 75 μm) for large catalyst loading. The choice would certainly be different if more precious catalyst, like a Rh-based one, was used in microchannel reactor. Under that condition, the weight of catalyst productivity is larger in economic evaluation, and the catalyst usage deteriorates more rapidly with increasing washcoat thickness due to faster intrinsic kinetics. The cost-effective solution could then be speculated to be a small washcoat dimension that ensures high catalyst productivity.

Conclusions

Washcoat-resolved simulation of a microchannel reactor has been performed concerning alumina supported Ni-based catalyst, using detailed chemistry of SMR and 2-D CFD models. The model properly described and revealed the kinetic-transport interactions for both the bulk gas phase and the porous washcoat phase. The flow, temperature and concentration fields, and the basics of the coupling between reaction and internal mass transfer have been investigated theoretically, followed by further discussion on the optimization of washcoat involving its dimension, pore diameter and porosity subject to process demands. The major conclusions are:

- In a microchannel reactor which is wall-coated with typical alumina supported catalysts, the interior axial velocity profile is approximately parabolic in the gas phase, while resembles plug flow within the washcoat. Thicker washcoat leads to reduced gas-phase residence time at a constant inlet volumetric flow. With increased permeability, viscous momentum transfer is intensified at the gas phase - porous media interface, leading to increased velocity gradient within the washcoat.

Please cite this article in press as: Cao C, et al., Numerical analysis on steam methane reforming in a plate microchannel reactor: Effect of washcoat properties, International Journal of Hydrogen Energy (2016), http://dx.doi.org/10.1016/j.ijhydene.2016.09.034

However, convective mass transfer is always trivial compared with diffusion, which dominates mass transfer into washcoat.

- Microchannel reactor has superb heat transfer and external mass transfer performance in the transverse direction. Rapid heat-up of feedstock to wall temperature is completed within a negligibly short region right after the entrance, which shows no sign of reduction with a thick washcoat of 100 μm. Species concentration gradients in the bulk gas phase is minute.
- SMR over Ni-based catalyst in a microchannel reactor is under mixed control of reaction and mass transfer within washcoat. High initial rate of reforming leads to unavoidable, considerable internal mass transfer resistance in the entrance region, even for a thin washcoat of 10 μm. Nonetheless, the catalyst usage with a typical washcoat thickness of 25 μm is no less than 80% at all temperatures with all catalyst loadings, being 1–2 orders of magnitude higher than that used in fixed-bed reactors.
- Washcoat structure, especially pore diameter, has significant impact on the heat coupling of an integrated microchannel reactor. Washcoat containing larger fraction of macropores (having large mean pore diameter) contributes to better heat match through enhancing internal mass transfer, which lowers the hotspot temperature and axial temperature gradients in the anterior part of the reactor. By contrast, the role of porosity is minor.
- Using thicker catalytic washcoat to carry a greater loading of catalyst is feasible for increasing the reactor throughput within washcoat thickness of 75 μm, at the expense of certain loss of catalyst productivity. While this trade-off is cost-efficient for the moderate-price Ni-based catalyst, the solution could not be migrated to noble metal catalysts. Overall, optimization of washcoat properties must consider synthetically the catalyst activity and the overall economics influenced by catalyst price.

Acknowledgement

This work was financially supported by PetroChina.

Nomenclature

x	Length in x direction, m
y	Length in y direction, m
u	Velocity, m/s
P	Pressure, Pa
C	Species concentration, $kmol \cdot m^{-3}$
h	Molar enthalpy, $kJ \cdot mol^{-1}$
k	Thermal conductivity, $W \cdot m^{-1} \cdot K^{-1}$
T	Temperature, K
N	Number
J	Diffusive mass flux, $kg \cdot m^{-2} \cdot s^{-1}$
C_p	Specific heat, $J \cdot g^{-1} \cdot K^{-1}$
X	Molar fraction
Y	Mass fraction
D	Mass diffusivity, $m^2 \cdot s^{-1}$
M	Molecular weight, $kg \cdot mol^{-1}$
R	Universal gas constant, $J \cdot mol^{-1} \cdot K^{-1}$
k_B	Boltzmann constant, $J \cdot K^{-1}$
S	Source terms in momentum and energy conservation equations
d	Diameter, m
R	Mass rate of reaction on a per washcoat volume basis, $kg \cdot m^{-3} \cdot s^{-1}$
$\widehat{R}$	Molar rate of reaction on a per washcoat volume basis, $mol \cdot m^{-3} \cdot s^{-1}$
r	Creating or consuming rate of each species in combustion, $kmol \cdot m^{-2} \cdot s^{-1}$
k_n	Rate constant of the nth elementary reactions of SMR, in [cm, mol, s]
$\widehat{r}$	Molar rate of reaction on a per surface area basis, $mol \cdot cm^{-2} \cdot s^{-1}$
A	Pre exponential factor, cm, mol, s;
E_a	Activation energy, $kJ \cdot mol^{-1}$
e	Activation energy modified by surface coverage, $kJ \cdot mol^{-1}$
r_c	Reaction rate of CH_4 catalytic combustion, $kmol \cdot kg_{cat}^{-1} \cdot h^{-1}$
k_c	Reaction rate constants of CH_4 catalytic combustion, $kmol \cdot kg_{cat}^{-1} \cdot h^{-1} \cdot bar^{-1.5}$
K^C	Adsorption constant, bar^{-1}
F	Surface area, m^2
w	Weight percent
L	Total length of catalyst bed, m

Greek letters

ρ	Density, $kg \cdot m^{-3}$
μ	Viscosity, Pa·s
κ	Permeability, m^2
σ_i	Collision diameter of the ith species, Å
ε_i	Characteristic Lenard–Jones energy of the ith species, J
γ	Viscosity coefficient
Ω_D	Collision integral
δ	Thickness, m
ε	Porosity
τ	Tortuosity
Θ	Surface coverage
φ	Exponent of surface coverage
α	Temperature exponent
τ_n	Number of active sites occupied by adsorpted species in the nth elementary reaction of SMR
υ	Stoichiometric coefficient
Γ	Density of active sites, $mol \cdot cm^{-2}$
η	Effectiveness factor

Subscripts

eff	Effective
avg	Average
cat	Catalyst
su	Superficial
phy	Physical
H	Heat
M	Momentum, molecular

Please cite this article in press as: Cao C, et al., Numerical analysis on steam methane reforming in a plate microchannel reactor: Effect of washcoat properties, International Journal of Hydrogen Energy (2016), http://dx.doi.org/10.1016/j.ijhydene.2016.09.034

w	Wall
k	Knudsen
p	Pore
g	Gas phase
f	Fluid
s	Solid; Surface
i,j	The ith species
n	The nth elementary reaction
C	Driven by concentration gradients
T	Driven by temperature gradients

Appendix

1 Physical properties

The viscosity of each gas species and the gas mixture were calculated using Chapman–Enskog's kinetic theory and the mixed gas formula [43].

$$\mu_i = 2.6693 \times 10^{-6} \frac{\sqrt{M_i T}}{\sigma^2 \Omega_{\mu,i}} \tag{A.1}$$

$$\mu_f = \sum_{i=1}^{N_g} \frac{X_i \mu_i}{\sum_{j=1}^{N_g} X_j \frac{1}{\sqrt{8}} \left(1 + \frac{M_i}{M_j}\right)^{-0.5} \left[1 + \left(\frac{\mu_i}{\mu_j}\right)^{0.5} \left(\frac{M_j}{M_i}\right)^{0.25}\right]^2} \tag{A.2}$$

The heat capacity of each species $c_{p,i}$ was computed by polynomial correlations. The thermal conductivity of gas species i was computed by Chapman–Enskog's kinetic theory [43]:

$$k_i = \frac{15}{4} \frac{R}{M_i} \mu_i \left[\frac{4}{15} \frac{c_{p,i} M_i}{R} + \frac{1}{3}\right] \tag{A.3}$$

The heat capacity and thermal conductivity of gas mixture were calculated by mass-weighted mixing-law:

$$c_{p,f} = \sum_i Y_i c_{p,i} \tag{A.4}$$

$$k_f = \sum_i Y_i k_i \tag{A.5}$$

The binary diffusivity D_{ij} and thermal diffusivity $D_{i,T}$ were calculated as [43,68]:

$$D_{ij} = 0.001858 T^{3/2} \frac{\left(1/M_i + 1/M_j\right)^{1/2}}{P \sigma_{ij}^2 \Omega_D} \tag{A.6}$$

$$D_{i,T} = -2.59 \times 10^{-7} T^{0.659} \left[\frac{M_i^{0.511} X_i}{\sum_{i=1}^{N_g} M_i^{0.511} X_i} - Y_i\right] \cdot \left[\frac{\sum_{i=1}^{N_g} M_i^{0.511} X_i}{\sum_{i=1}^{N_g} M_i^{0.489} X_i}\right] \tag{A.7}$$

where $\sigma_{ij} = (\sigma_i + \sigma_j)/2$ is the arithmetic average of the collision diameters; Ω_D is the collision integral, computed by:

$$\Omega_D = \frac{A}{T_N^B} + \frac{C}{\exp(DT_N)} + \frac{E}{\exp(FT_N)} + \frac{G}{\exp(HT_N)} \tag{A.8}$$

in which $A = 1.06036$, $B = 0.1561$, $C = 0.193$, $D = 0.47635$, $E = 1.03587$, $F = 1.52996$, $G = 1.76474$, $H = 3.89411$; T_N was given in

$$T_N = \frac{k_B T}{\varepsilon_{ij}} \tag{A.9}$$

where k_B is the Boltzmann constant and $\varepsilon_{ij} = (\varepsilon_i \varepsilon_j)^{1/2}$ is the geometric average of the characteristic Lenard–Jones energies.

2 Microkinetics model

Table A.1 – Microkinetics of SMR on Ni catalyst [45].

Elementary reactions		A/[cm, mol, s]	E_a/[kJ/mol]
Adsorption reactions	(R1)H_2 + Ni(s) + Ni(s) → H(s) + H(s)	0.01	0
	(R2)O_2 + Ni(s) + Ni(s) → O(s) + O(s)	0.01	0
	(R3)CH_4 + Ni(s) → CH_4(s)	0.008	0
	(R4)H_2O + Ni(s) → H_2O(s)	0.1	0
	(R5)CO_2 + Ni(s) → CO_2(s)	1E-5	0
	(R6)CO + Ni(s) → CO(s)	0.5	0
Desorption reactions	(R7)H(s) + (7)H(s) → H_2 + Ni(s) + Ni(s)	2.545E19	81.21
	(R8)O(s) + O(s) → O_2 + Ni(s) + Ni(s)	4.283E23	474.95
	(R9)H_2O(s) → H_2O + Ni(s)	3.732E12	60.79
	(R10)CO(s) → CO + Ni(s)	3.563E11	111.27−50$\theta_{CO(s)}$
	(R11)CO_2(s) → CO_2 + Ni(s)	6.447E7	25.98
	(R12)CH_4(s) → CH_4 + Ni(s)	8.705E15	37.55
	(R13)H(s) + O(s) → OH(s) + Ni(s)	5.0E22	97.9
	(R14)OH(s) + Ni(s) → H(s) + O(s)	1.781E21	36.09
	(R15)H(s) + OH(s) → H_2O(s) + Ni(s)	3.0E20	42.7
	(R16)H_2O(s) + Ni(s) → H(s) + OH(s)	2.271E21	91.76
	(R17)OH(s) + OH(s) → H_2O(s) + O(s)	3.0E21	100
	(R18)H_2O(s) + O(s) → OH(s) + OH(s)	6.373E23	210.86

Please cite this article in press as: Cao C, et al., Numerical analysis on steam methane reforming in a plate microchannel reactor: Effect of washcoat properties, International Journal of Hydrogen Energy (2016), http://dx.doi.org/10.1016/j.ijhydene.2016.09.034

Table A.1 – (*continued*)

Elementary reactions		A/[cm, mol, s]	E_a/[kJ/mol]
Surface reactions	(R19)C(s) + O(s) → CO(s) + Ni(s)	5.2E23	148.1
	(R20)CO(s) + Ni(s) → C(s) + O(s)	1.354E22	$116.12-50\theta_{CO(s)}$
	(R22)CO_2(s) + Ni(s) → CO(s) + O(s)	4.653E23	89.32
	(R23)CH_4(s) + Ni(s) → CH_3(s) + H(s)	3.7E21	57.7
	(R24)CH_3(s) + H(s) → CH_4(s) + Ni(s)	6.034E21	61.58
	(R25)CH_3(s) + Ni(s) → CH_2(s) + H(s)	3.7E24	100.0
	(R26)CH_2(s) + H(s) → CH_3(s) + Ni(s)	1.293E22	55.33
	(R27)CH_2(s) + Ni(s) → CH(s) + H(s)	3.7E24	97.1
	(R28)CH(s) + H(s) → CH_2(s) + Ni(s)	4.089E24	79.18
	(R29)CH(s) + Ni(s) → C(s) + H(s)	3.7E21	18.8
	(R30)C(s) + H(s) → CH(s) + Ni(s)	4.562E22	161.11
	(R31)CH_4(s) + O(s) → CH_3(s) + OH(s)	1.7E24	88.3
	(R32)CH_3(s) + OH(s) → CH_4(s) + O(s)	9.876E22	30.37
	(R33)CH_3(s) + O(s) → CH_2(s) + OH(s)	3.7E24	130.1
	(R34)CH_2(s) + OH(s) → CH_3(s) + O(s)	4.607E21	23.62
	(R35)CH_2(s) + O(s) → CH(s) + OH(s)	3.7E24	126.8
	(R36)CH(s) + OH(s) → CH_2(s) + O(s)	1.457E23	47.07
	(R37)CH(s) + O(s) → C(s) + OH(s)	3.7E21	48.1
	(R38)C(s) + OH(s) → CH(s) + O(s)	1.625E21	128.61
	(R39)HCO(s) + Ni(s) → CO(s) + H(s)	3.7E21	$50\theta_{CO(s)}$
	(R40) CO(s) + H(s) → HCO(s) + Ni(s)	4.019E20	132.23
	(R41) HCO(s) + Ni(s) → CH(s) + O(s)	3.7E24	95.8
	(R42) CH(s) + O(s) → HCO(s) + Ni(s)	4.604E20	109.97

The site density of Ni is 2.6×10^{-9} mol·cm^{-2}; the rate constants for adsorption reactions are given in sticking coefficients.

REFERENCES

[1] Rostrup-Nielsen J. Steam reforming of hydrocarbons. A historical perspective. In: Xinhe B, Yide X, editors. Stud surf sci catal. Elsevier; 2004. p. 121–6.
[2] Vlachos DG, Caratzoulas S. The roles of catalysis and reaction engineering in overcoming the energy and the environment crisis. Chem Eng Sci 2010;65:18–29.
[3] Rostrup-Nielsen Jens R. Catalytic steam reforming. Catal Sci Technol 1984;5:1–117.
[4] Tracz E, Scholz R, Borowiecki T. High-resolution electron microscopy study of the carbon deposit morphology on nickel catalysts. Appl Catal 1990;66:133–47.
[5] Renken A, Kiwi-Minsker L. Chapter 2-Microstructured catalytic reactors. In: Bruce CG, Helmut K, editors. Adv catal. Academic Press; 2010. p. 47–122.
[6] Holladay JD, Wang Y, Jones E. Review of developments in portable hydrogen production using microreactor technology. Chem Rev 2004;104:4767–89.
[7] Rostrup-Nielsen T. Manufacture of hydrogen. Catal Today 2005;106:293–6.
[8] Tonkovich ALY, Wang Y. Overview of early-stage microchannel reactor development at Pacific Northwest National Laboratory. American Chemical Society; 2005.
[9] Tonkovich AY, Perry S, Wang Y, Qiu D, LaPlante T, Rogers WA. Microchannel process technology for compact methane steam reforming. Chem Eng Sci 2004;59:4819–24.
[10] Tonkovich ALY, Yang B, Perry ST, Fitzgerald SP, Wang Y. From seconds to milliseconds to microseconds through tailored microchannel reactor design of a steam methane reformer. Catal Today 2007;120:21–9.
[11] Wang Y, Chin YH, Rozmiarek RT, Johnson BR, Gao Y, Watson J, et al. Highly active and stable Rh/MgO-Al2O3 catalysts for methane steam reforming. Catal Today 2004;98:575–81.
[12] Farrauto R, Hwang S, Shore L, Ruettinger W, Lampert J, Giroux T, et al. New material needs for hydrocarbon fuel processing: generating hydrogen for the PEM fuel cell. Annu Rev Mater Res 2003;33:1–27.
[13] Stefanidis GD, Vlachos DG. Intensification of steam reforming of natural gas: choosing combustible fuel and reforming catalyst. Chem Eng Sci 2010;65:398–404.
[14] Stutz MJ, Poulikakos D. Optimum washcoat thickness of a monolith reactor for syngas production by partial oxidation of methane. Chem Eng Sci 2008;63:1761–70.
[15] von Rickenbach J, Lucci F, Narayanan C, Dimopoulos Eggenschwiler P, Poulikakos D. Effect of washcoat diffusion resistance in foam based catalytic reactors. Chem Eng J 2015;276:388–97.
[16] Stefanidis GD, Vlachos DG. Millisecond methane steam reforming via process and catalyst intensification. Chem Eng Technol 2008;31:1201–9.
[17] Horn R, Williams KA, Degenstein NJ, Bitsch-Larsen A, Nogare DD, Tupy SA, et al. Methane catalytic partial oxidation on autothermal Rh and Pt foam catalysts: oxidation and reforming zones, transport effects, and approach to thermodynamic equilibrium. J Catal 2007;249:380–93.
[18] Mbodji M, Commenge JM, Falk L. Preliminary design and simulation of a microstructured reactor for production of synthesis gas by steam methane reforming. Chem Eng Res Des 2014;92:1728–39.
[19] Yuan J, Ren F, Sunden B. Analysis of chemical-reaction-coupled mass and heat transport phenomena in a methane reformer duct for PEMFCs. Int J Heat Mass Transf 2007;50:687–701.
[20] Arzamendi G, Dieguez PM, Montes M, Odriozola JA, Sousa-Aguiar EF, Gandia LM. Methane steam reforming in a microchannel reactor for GTL intensification: a computational fluid dynamics simulation study. Chem Eng J 2009;154:168–73.
[21] Arzamendi G, Uriz I, Navajas A, Diéguez PM, Gandía LM, Montes M, et al. A CFD study on the effect of the characteristic dimension of catalytic wall microreactors. AIChE J 2012;58:2785–97.

Please cite this article in press as: Cao C, et al., Numerical analysis on steam methane reforming in a plate microchannel reactor: Effect of washcoat properties, International Journal of Hydrogen Energy (2016), http://dx.doi.org/10.1016/j.ijhydene.2016.09.034

[22] Jeon SW, Yoon WJ, Jeong MW, Kim Y. Optimization of a counter-flow microchannel reactor using hydrogen assisted catalytic combustion for steam reforming of methane. Int J Hydrogen Energy 2014;39:6470–8.
[23] Murphy DM, Manerbino A, Parker M, Blasi J, Kee RJ, Sullivan NP. Methane steam reforming in a novel ceramic microchannel reactor. Int J Hydrogen Energy 2013;38:8741–50.
[24] Blakeley B, Sullivan N. Fuel processing in a ceramic microchannel reactor: expanding operating windows. Int J Hydrogen Energy 2016;41:3794–802.
[25] Deutschmann O. Modeling of the interactions between catalytic surfaces and gas-phase. Catal Lett 2015;145:272–89.
[26] Irani M, Alizadehdakhel A, Pour AN, Hoseini N, Adinehnia M. CFD modeling of hydrogen production using steam reforming of methane in monolith reactors: surface or volume-base reaction model? Int J Hydrogen Energy 2011;36:15602–10.
[27] Mladenov N, Koop J, Tischer S, Deutschmann O. Modeling of transport and chemistry in channel flows of automotive catalytic converters. Chem Eng Sci 2010;65:812–26.
[28] Vaccaro S, Malangone L, Ciambelli P. Modelling of a catalytic micro-reactor coupling endothermic methane reforming and combustion. Int J Chem React Eng 2010;8.
[29] Zanfir M, Baldea M, Daoutidis P. Optimizing the catalyst distribution for countercurrent methane steam reforming in plate reactors. AIChE J 2011;57:2518–28.
[30] Ni M. 2D heat and mass transfer modeling of methane steam reforming for hydrogen production in a compact reformer. Energy Convers Manage 2013;65:155–63.
[31] Jeon SW, Yoon WJ, Baek C, Kim Y. Minimization of hot spot in a microchannel reactor for steam reforming of methane with the stripe combustion catalyst layer. Int J Hydrogen Energy 2013;38:13982–90.
[32] Murphy DM, Parker M, Sullivan NP. The interplay of heat transfer and endothermic chemistry within a ceramic microchannel reactor. J Therm Sci Eng Appl 2014;6:031007.
[33] Lakhete P, Janardhanan VM. Modeling process intensified catalytic plate reactor for synthesis gas production. Chem Eng Sci 2014;110:13–9.
[34] Xu J, Froment GF. Methane steam reforming, methanation and water-gas shift: I. Intrinsic kinetics. AIChE J 1989;35:88–96.
[35] Ding S, Wu C, Cheng Y, Jin Y, Cheng Y. Analysis of catalytic partial oxidation of methane on rhodium-coated foam monolith using CFD with detailed chemistry. Chem Eng Sci 2010;65:1989–99.
[36] Zhai X, Ding S, Cheng Y, Jin Y, Cheng Y. CFD simulation with detailed chemistry of steam reforming of methane for hydrogen production in an integrated micro-reactor. Int J Hydrogen Energy 2010;35:5383–92.
[37] Cao C, Zhang N, Chen X, Cheng Y. A comparative study of Rh and Ni coated microchannel reactor for steam methane reforming using CFD with detailed chemistry. Chem Eng Sci 2015;137:276–86.
[38] Zhou L, Guo Y, Yagi M, Sakurai M, Kameyama H. Investigation of a novel porous anodic alumina plate for methane steam reforming: hydrothermal stability, electrical heating possibility and reforming reactivity. Int J Hydrogen Energy 2009;34:844–58.
[39] Zhai X, Cheng Y, Zhang Z, Jin Y, Cheng Y. Steam reforming of methane over Ni catalyst in micro-channel reactor. Int J Hydrogen Energy 2011;36:7105–13.
[40] Chiuta S, Everson RC, Neomagus HWJP, Le Grange LA, Bessarabov DG. A modelling evaluation of an ammonia-fuelled microchannel reformer for hydrogen generation. Int J Hydrogen Energy 2014;39:11390–402.
[41] JPd Plessis, Diedericks GPJ. Pore-scale modelling of interstitial transport phenomena. In: Du Plessis JP, editor. Fluid transport in porous media. Southampton: Computational Mechanics Publications; 1997. p. 61–104.
[42] Janardhanan VM. A detailed approach to model transport, heterogeneous chemistry, and electrochemistry in solid-oxide fuel cells. [Dr.-Ing.]: Universität Karlsruhe (TH); 2007.
[43] Bird RB, Stewart WE, Lightfoot EN. Transport phenomena. New York: Wiley; 1960.
[44] Smoluchowski Mv. Zur kinetischen Theorie der Transpiration und Diffusion verdünnter Gase. Ann Phys 1910;338:1559–70.
[45] Hecht ES, Gupta GK, Zhu H, Dean AM, Kee RJ, Maier L, et al. Methane reforming kinetics within a Ni–YSZ SOFC anode support. Appl Catal a-Gen 2005;295:40–51.
[46] Janardhanan VM, Deutschmann O. CFD analysis of a solid oxide fuel cell with internal reforming: coupled interactions of transport, heterogeneous catalysis and electrochemical processes. J Power Sources 2006;162:1192–202.
[47] Maier L, Schädel B, Herrera Delgado K, Tischer S, Deutschmann O. Steam reforming of methane over nickel: development of a multi-step surface reaction mechanism. Top Catal 2011;54:845–58.
[48] Ma L, Trimm DL, Jiang C. The design and testing of an autothermal reactor for the conversion of light hydrocarbons to hydrogen .1. The kinetics of the catalytic oxidation of light hydrocarbons. Appl Catal a-Gen 1996;138:275–83.
[49] Trimm DL, Lam CW. The combustion of methane on platinum-alumina fiber catalysts .1. Kinetics and mechanism. Chem Eng Sci 1980;35:1405–13.
[50] Tan H, Pillai KM. Finite element implementation of stress-jump and stress-continuity conditions at porous-medium, clear-fluid interface. Comput Fluids 2009;38:1118–31.
[51] Beeckman JW. Measurement of the effective diffusion-coefficient of nitrogen monoxide through porous monolith-type ceramic catalysts. Ind Eng Chem Res 1991;30:428–30.
[52] Xu J, Froment GF. Methane steam reforming: II. Diffusional limitations and reactor simulation. AIChE J 1989;35:97–103.
[53] Hayes RE, Kolaczkowskib ST, Li PKC, Awdry S. Evaluating the effective diffusivity of methane in the washcoat of a honeycomb monolith. Appl Catal B Environ 2000;25:93–104.
[54] Bader G, Deuflhard P. A semi-implicit midpoint rule for stiff systems of ordinary differential-equations. Numer Math 1983;41:373–98.
[55] de Smet CRH, de Croon MHJM, Berger RJ, Marin GB, Schouten JC. Design of adiabatic fixed-bed reactors for the partial oxidation of methane to synthesis gas. Application to production of methanol and hydrogen-for-fuel-cells. Chem Eng Sci 2001;56:4849–61.
[56] Numaguchi T, Kikuchi K. Intrinsic kinetics and design simulation in a complex-reaction network - steam-methane reforming. Chem Eng Sci 1988;43:2295–301.
[57] Stefanidis GD, Vlachos DG, Kaisare NS, Maestri M. Methane steam reforming at microscales: operation strategies for variable power output at millisecond contact times. AIChE J 2009;55:180–91.
[58] Elnashaie SSEH, Abashar MEE. Steam reforming and methanation effectiveness factors using the dusty gas-model under industrial conditions. Chem Eng Process 1993;32:177–89.
[59] Rajesh JK, Gupta SK, Rangaiah GP, Ray AK. Multiobjective optimization of steam reformer performance using genetic algorithm. Ind Eng Chem Res 2000;39:706–17.
[60] Oh PP, Rangaiah GP, Ray AK. Simulation and multiobjective optimization of an industrial hydrogen plant based on refinery off-gas. Ind Eng Chem Res 2002;41:2248–61.
[61] Pantoleontos G, Kikkinides ES, Georgiadis MC. A heterogeneous dynamic model for the simulation and

Please cite this article in press as: Cao C, et al., Numerical analysis on steam methane reforming in a plate microchannel reactor: Effect of washcoat properties, International Journal of Hydrogen Energy (2016), http://dx.doi.org/10.1016/j.ijhydene.2016.09.034

optimisation of the steam methane reforming reactor. Int J Hydrogen Energy 2012;37:16346–58.
[62] De Falco M, Di Paola L, Marrelli L. Heat transfer and hydrogen permeability in modelling industrial membrane reactors for methane steam reforming. Int J Hydrogen Energy 2007;32:2902–13.
[63] Halabi MH, de Croon MHJM, van der Schaaf J, Cobden PD, Schouten JC. Modeling and analysis of autothermal reforming of methane to hydrogen in a fixed bed reformer. Chem Eng J 2008;137:568–78.
[64] Olivieri A, Vegliò F. Process simulation of natural gas steam reforming: fuel distribution optimisation in the furnace. Fuel Process Technol 2008;89:622–32.
[65] Kumar S, Kumar S, Prajapati JK. Hydrogen production by partial oxidation of methane: modeling and simulation. Int J Hydrogen Energy 2009;34:6655–68.
[66] Latham DA, McAuley KB, Peppley BA, Raybold TM. Mathematical modeling of an industrial steam-methane reformer for on-line deployment. Fuel Process Technol 2011;92:1574–86.
[67] Zanfir M, Gavriilidis A. Influence of flow arrangement in catalytic plate reactors for methane steam reforming. Chem Eng Res Des 2004;82:252–8.
[68] Kuo KKY. Principles of combustion. New York: John Wiley and Sons; 1986.

Please cite this article in press as: Cao C, et al., Numerical analysis on steam methane reforming in a plate microchannel reactor: Effect of washcoat properties, International Journal of Hydrogen Energy (2016), http://dx.doi.org/10.1016/j.ijhydene.2016.09.034